Mode-coupled emission from hBN flakes on metal-dielectric multilayers

Quantum Engineering Master's Degree Thesis

Author:
Marta Pipitone

Supervisor:
prof. Emiliano Descrovi

DISAT
Politecnico di Torino
27/11/2025

Politecnico di Torino

Acknowledgements

I want to thank my supervisor, Emiliano Descrovi, who made this thesis possible and always supported me in every possible way. Then, two other people who helped me a lot are Niccolò Marcucci and Zongyuan Tang: thanks for your time and kindness. I want to thank Giuseppe Leonetti too, who helped me with EBL at Inrim. Finally, I'm grateful for all the love and support from my family, friends and people from the third floor of Crocetta.

Abstract

The development of reliable and integrated single-photon sources (SPS) represents a key milestone toward the implementation of quantum communications and information technologies. In this framework, point-like lattice defects in hexagonal boron nitride (hBN) flakes has recently attracted significant attention as a promising solid-state emitter platform; thanks to its room-temperature operation, high photostability, and compatibility with on-chip photonic architectures. The aim of this work is to investigate the coupling of defect-related emission in hBN flakes with optical modes sustained by engineered multilayer structures, specifically metal-dielectric multilayers supporting Tamm plasmons (TPs) and dielectric multilayers supporting Bloch surface waves (BSWs).

This activity involves theoretical modeling, clean room fabrication and experimental optical characterization. Rigorous Coupled-Wave Analysis (RCWA) simulations are employed to calculate the optical response of multilayered structures. Electron beam lithography has been performed to fabricate sub-wavelength diffraction gratings on top of the multilayers, to facilitate the coupling with BSW modes. Hexagonal boron nitride flakes, prepared via mechanical exfoliation, are transferred onto the photonic structures and then indented with a heated AFM tip, to create local emitters. Finally, optical characterizations involving photoluminescence and white-light spectral measurements in both direct and Fourier space are performed.

The integration of hBN emitters with Bloch surface wave platforms and Tamm Plasmon structures is explored as a potential route to achieve enhanced emission directionality and improved coupling efficiency. Although further optimization and characterization are required, the presented results demonstrate the feasibility of hybrid hBN–multilayer systems as a versatile platform for the implementation of integrated quantum photonic devices upon optical pumping.

Contents

List of Figures

Chapter 1

Introduction

The advent of quantum technologies has spurred a significant interest in developing reliable, on-demand single-photon sources (SPS). These sources are crucial for applications such as quantum key distribution, quantum computing, and photonic quantum simulations, where the ability to manipulate individual photons determines both performance and security. Among the various SPS platforms, defects in hexagonal boron nitride (hBN) have attracted attention due to their ability to provide stable single-photon emission at room temperature [6]. This property makes hBN especially promising for creating compact, integrable quantum photonic devices that could revolutionize practical quantum communication systems.
Despite the promising outlook, hBN-based SPSs face several technical challenges. Key issues include:

- Emitter consistency: achieving uniform defect quality and reproducible emission characteristics remains a challenge.
- Photon purity and brightness: maximizing the photon extraction efficiency and ensuring high single-photon purity are critical for reliable operation.
- Scalability and integration: developing scalable fabrication processes and integrating hBN emitters with existing photonic circuits require advanced material engineering and process optimization.

Moreover, when compared to other SPS implementations, such as quantum dots, spontaneous parametric down-conversion (SPDC) sources, and color centers in diamond, each platform presents its trade-offs. While quantum dots can offer near-deterministic photon emission, they often require cryogenic conditions. Similarly, although NV centers in diamond are highly photostable, integrating them into on-chip architectures proves challenging. hBN, with its room-temperature operation and inherent two-dimensional nature, offers a compelling alternative, although overcoming its consistency and integration issues is paramount for practical applications.

The coupling between the multilayer and the hBN defect is yet another challenge, since some kind of surface mode must be exploited. In this work we focus on two possible alternatives:

- **Tamm Plasmon (TP)**: surface state localized at the interface between a metal and a photonic crystal.
- **Bloch Surface Waves (BSW)**: electromagnetic mode propagating along the surface of a dielectric multilayer.

In the following chapters I'll explain the main physical concepts and photonic structures in chapter 2, the methods and tools used to simulate the behaviour of the photonic devices in chapter 3, the followed experimental procedure step by step to couple the TP/BSW to hBN in chapter 4, then I'll analyze and discuss the obtained results in chapter 5 and finally I'll summarize everything in chapter 6, suggesting improvements for future research.

Chapter 2

Theoretical framework

2.1 Light-matter interaction

Electromagnetic waves in vacuum obey to the D'Alambèrt equation, derived from the well-known Maxwell's equations,

$$\nabla^2 \mathbf{E} = \mu_0 \varepsilon_0 \frac{\partial^2 \mathbf{E}}{\partial t^2} \tag{2.1}$$

where ε_0 is the vacuum electric permittivity and μ_0 is the vacuum magnetic permeability. The propagation speed in vacuum is constant and equal to the speed of light $c = \frac{1}{\sqrt{\mu_0 \varepsilon_0}}$.
In a generic medium, where we have to take into account also the relative magnetic permeability μ_r, the relative electric permittivity ε_r and the electrical conductivity σ, the wave equation is the following one:

$$\nabla^2 \mathbf{E} = \mu\varepsilon \frac{\partial^2 \mathbf{E}}{\partial t^2} + \mu\sigma \frac{\partial E}{\partial t} \tag{2.2}$$

If we're dealing with a dielectric medium, of course, $\sigma = 0$, therefore the previous equation simplifies:

$$\nabla^2 \mathbf{E} = \mu\varepsilon \frac{\partial^2 \mathbf{E}}{\partial t^2} \tag{2.3}$$

So, light waves propagate at different speeds inside different mediums, since now the propagation speed is $v = \frac{1}{\sqrt{\mu\varepsilon}} = \frac{1}{\sqrt{\varepsilon_r}} \frac{1}{\sqrt{\mu_0 \varepsilon_0}} = \frac{c}{n}$, where we have defined the material's refractive index $n = \sqrt{\varepsilon_r}$, considering $\mu_r = 1$ (non-magnetic material).
If we consider an isotropic material, it's possible to express the solution of the D'Alambèrt equation as the product of a space dependent component and a time dependent component.

$$\mathbf{E}(\mathbf{r}, t) \propto U(\mathbf{r}) F(t) \tag{2.4}$$

Assuming an harmonic time dependence $F(t) = e^{-i\omega t}$, the previous equation simplifies

into:

$$\nabla^2 U(\mathbf{r}) = \frac{n^2}{c^2}(-\omega^2)U(\mathbf{r}) \tag{2.5}$$

Now, the easiest solution for this type of wave equation is found in the form of plane waves.

$$U(\mathbf{r}) = e^{i\mathbf{k}\cdot\mathbf{r}} \tag{2.6}$$

They're characterized by a planar wavefront and they propagate in the direction given by the wavevector **k**.
By substituting this solution into eq. 2.5, we find the photon dispersion relationship:

$$k = \frac{n}{c}\omega \tag{2.7}$$

Considering that the angular frequency is defined as $\omega = \frac{2\pi}{T}$ and the wavelength as $\lambda = \frac{c}{n}T$, where T is the time period, the wavevector can be expressed as

$$k = \frac{2\pi}{\lambda} \tag{2.8}$$

Let's now analyze what happens to light at the interface between two different dielectric materials, for example air ($n_1 = 1$) and glass ($n_2 = 1.5$), and assume that the wave is initially travelling in air and impinges on the glass' surface with an incidence angle θ_1 with respect to the interface normal. Notice that both the wavelength and the wavevector depend on the refractive index of the medium:

$$\lambda = \frac{\lambda_0}{n} \tag{2.9}$$

$$k = k_0 n \tag{2.10}$$

where λ_0 and k_0 are referred to the vacuum.

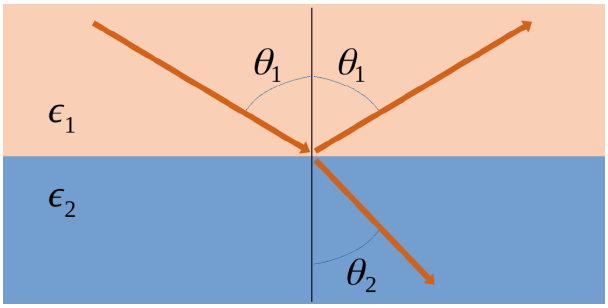

Figure 2.1: Schematic of a planewave impinging with an angle θ_1 on the interface between two different materials.[6]

We introduce now the concepts of reflectance R and transmittance T, as the proportion of incident light at a specific frequency that is respectively reflected or transmitted. In

an ideal loss-less material the energy conservation law tells us that $R+T=1$, while in a real lossy material we have that $R+T+A=1$, which takes into account also the fraction of light that is absorbed by the material. When considering the interface between two different dielectrics what happens, in general, is that part of the wave is reflected back into the first medium at θ_1 and the rest of it is transmitted into the second medium at the refraction angle θ_2. Moreover, the tangential components of wavevector and electric field are conserved, so $k_{1//} = k_{2//}$ and $E_{1//} = E_{2//}$.
From this we derive the Snell's law, which connects the refraction angle and the incidence angle:

$$n_1 sin(\theta_1) = n_2 sin(\theta_2) \tag{2.11}$$

If $n_1 > n_2$ and $\theta_1 > \theta_c$, which is called critical angle and is defined as $\theta_c = sin^{-1}(\frac{n_2}{n_1})$, the incoming light will be completely reflected back into the first medium, since the refraction angle doesn't allow for propagation inside the second medium ($\theta_2 > \frac{\pi}{2}$). This phenomenon, called Total Internal Reflection (TIR), allows to confine light in a specific space region and is the basic working principle of waveguides. Inside a waveguide the dispersion is strongly non-linear, but we can define anyway an effective refractive index, such that: $k = n_{eff}(\omega)k_0$ So, the propagation inside the waveguide can be approximated to a planewave propagating inside a homogeneous material with refractive index equal to n_{eff}.

2.1.1 Light propagation in stratified media

Building on the plane-wave solutions and Snell's law introduced above (Eqs. 2.6 and 2.11), we consider a stack of m homogeneous, isotropic layers placed between an incident medium (index n_1) and a semi-infinite substrate (index n_s). Each layer j has refractive index n_j and thickness d_j. In general, n_j is complex: the real part describes the phase evolution (propagation), while the imaginary one is responsible for amplitude attenuation (absorption). Assume that a plane wave $E_{in} = E_1^+$ is incident on the first layer of the structure, and remember that in general a wave is represented by the sum of a forward propagating wave and a backwards propagating one.

$$E_i(z) = E_i^+ e^{jkz} + E_i^- e^{-jkz} \tag{2.12}$$

Now we need to consider that, at each interface, the incident wave is partially transmitted and partially reflected, but since there are multiple interfaces, the overall reflection/transmission of a stratified media is the sum of an infinite number of reflected/transmitted waves. The fields at the two faces of layer j are related by the 2×2 characteristic matrix

$$\begin{pmatrix} E_i^+ \\ E_i^- \end{pmatrix} = T_{i,j} \begin{pmatrix} E_j^+ \\ E_j^- \end{pmatrix}, \tag{2.13}$$

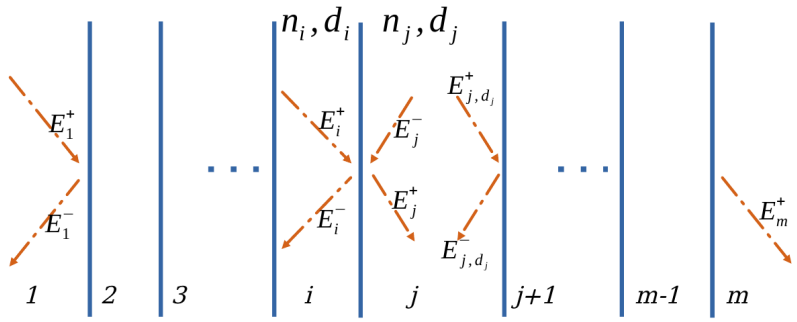

Figure 2.2: Schematic representation of a wave propagating in a stratified media.[6]

Then, taking into account also the propagation inside layer j, described by a matrix P_j, we can relate the field right before the next interface E_{j,d_j}, the one between layer j and j+1, to the field of layer i:

$$E_i = T_{i,j} P_j E_{j,d_j} \tag{2.14}$$

It's quite straightforward now to see that one can build the overall transfer matrix, by repeating this process for each layer and interface.

$$M = (\prod_{i=1}^{m-2} T_{i,i+1} P_{i+1}) T_{m-1,m} = \begin{pmatrix} M_{11} & M_{12} \\ M_{21} & M_{22} \end{pmatrix}. \tag{2.15}$$

This is called **Transfer Matrix Method (TMM)** and allows to express a relationship between the field on the right most side of the multilayer and the field on the left most side:

$$E_1 = M E_m \tag{2.16}$$

If the substrate is semi-infinite there will be only a forward wave, meaning that $E_m^- = 0$. Now, we can calculate the reflection and transmission coefficient of the (lossless) multilayer, remembering that $E_{in} = E_1^+$, $E_r = E_1^-$ and $E_t = E_m^+$.
By definition,

$$r = \frac{E_1^-}{E_1^+}, \qquad t = \frac{E_m^+}{E_1^+} \tag{2.17}$$

By solving eq. 2.16, it's possible to rewrite eq. 2.17 in terms of the transfer matrix elements.

$$r = \frac{M_{21}}{M_{11}}, \qquad t = \frac{1}{M_{11}} \tag{2.18}$$

Notice that the measurable reflectance and transmittance can be obtained as the square modulus of the previously calculated coefficients.

$$R = |r|^2, \qquad T = |t|^2 \tag{2.19}$$

2.2 Photonic crystals

Photonic crystals (PC) are engineered materials in which the refractive index is modulated periodically on a length scale comparable to the wavelength of light. This periodic modulation gives rise to photonic band gaps, ranges of wavelengths where light cannot propagate through the material. The concept is similar to the electronic band gaps in semiconductors, and it enables the control of light propagation, making these materials useful for a variety of optical applications such as waveguides, lasers, and filters. Photonic crystals can be one, two or three dimensional, depending on how many periodic directions there are.

There's a strong parallelism between the electrons in a crystalline semiconductor with a periodic electric potential and the photons traveling inside a dielectric structure within a periodic refractive index. Indeed, we can apply Bloch's theorem and express the solutions of Maxwell's equation in the following way:

$$U_{n,k_z,k_{//}}(\mathbf{r}) = e^{i\mathbf{k}_{//}\cdot(x,y)} e^{ik_z z} u_{n,k_z,k_{//}}(z) \tag{2.20}$$

The Bloch function has the same period Λ of the crystal, therefore $u_{n,k_z,k_{//}}(z+\Lambda) = u_{n,k_z,k_{//}}(z)$. In this way we define an eigenvalue problem, whose solutions provide the dispersion relation of the modes allowed in the 1DPC. Therefore, we are also able to identify the edges of the photonic band gap (PBG), a range of frequencies for which propagation is forbidden. This implies a high reflectivity for the frequencies belonging to PBG, while we expect a very low reflectivity for the allowed modes, since these can travel through the overall structure. Notice that there exists a 1-to-1 correspondence between the mode dispersion and the reflectivity map only if we're considering a loss-less material, and only for the modes lying inside the light cone, which can then propagate in vacuum/air. The light cone is identified by $\omega = ck_{//}$ for both TE and TM polarizations. It can be useful to trace also the light cone of the substrate on which the 1DPC is placed, especially for the discussion in the following section.

Last but not least, it's important to remember that perfect infinitely periodic PCs can't exist, therefore also the PBG can't be perfect and defect modes will be present. In section 2.3 we will focus on two types of surface modes, and how these can be exploited to manipulate light in sophisticated ways.

2.2.1 Distributed Bragg Reflectors

A Distributed Bragg Reflector (DBR) is a one-dimensional PC composed of alternating layers of two dielectric materials with different refractive indexes. By means of constructive and destructive interference, the DBR exhibits high reflectivity over a specific spectral range, known as the **stop band**, centered around λ_0. Therefore, DBRs are widely used in optical filters, cavity mirrors, and in photonic crystal structures to enhance light confinement.

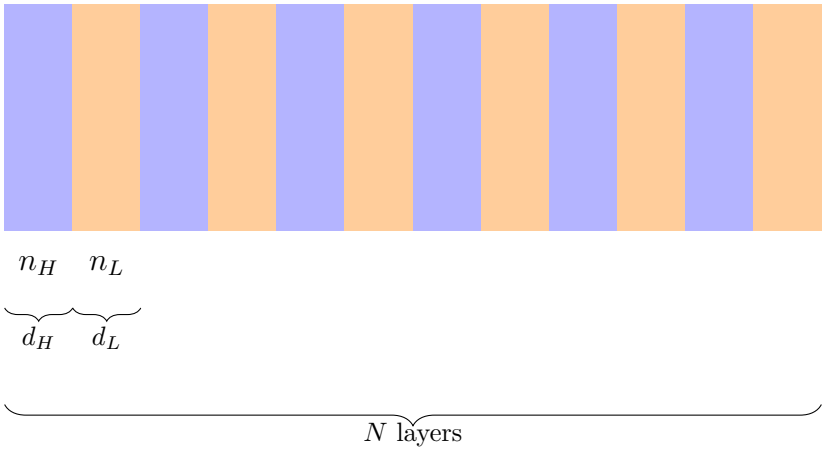

Figure 2.3: Schematic of a DBR with alternating high (n_H, thickness d_H) and low (n_L, thickness d_L) refractive index layers.

A DBR is typically designed so that each layer has an **optical thickness** equal to one quarter of the central wavelength λ_0 of the desired stop band:

$$n_H d_H = n_L d_L = \frac{\lambda_0}{4}, \tag{2.21}$$

where n_H and n_L are the refractive indexes of the high- and low-index materials, and d_H and d_L are the corresponding physical thicknesses. This configuration maximizes constructive interference for reflected waves and destructive interference for transmitted ones at λ_0, to which corresponds the so called Bragg frequency $\omega_0 = \frac{2\pi c}{\lambda_0}$. For a DBR composed of N pairs of layers, the normal-incidence reflectivity at the central wavelength can be approximated as [9]:

$$R \approx \left(\frac{n_H^{2N} - n_L^{2N}}{n_H^{2N} + n_L^{2N}} \right)^2, \tag{2.22}$$

assuming the structure is surrounded by a medium with refractive index equal to 1 (air or vacuum). The stop-band width $\Delta\lambda$ is determined by the refractive index contrast $n_H - n_L$:

$$\frac{\Delta\lambda}{\lambda_0} \approx \frac{4}{\pi} \arcsin\left(\frac{n_H - n_L}{n_H + n_L} \right). \tag{2.23}$$

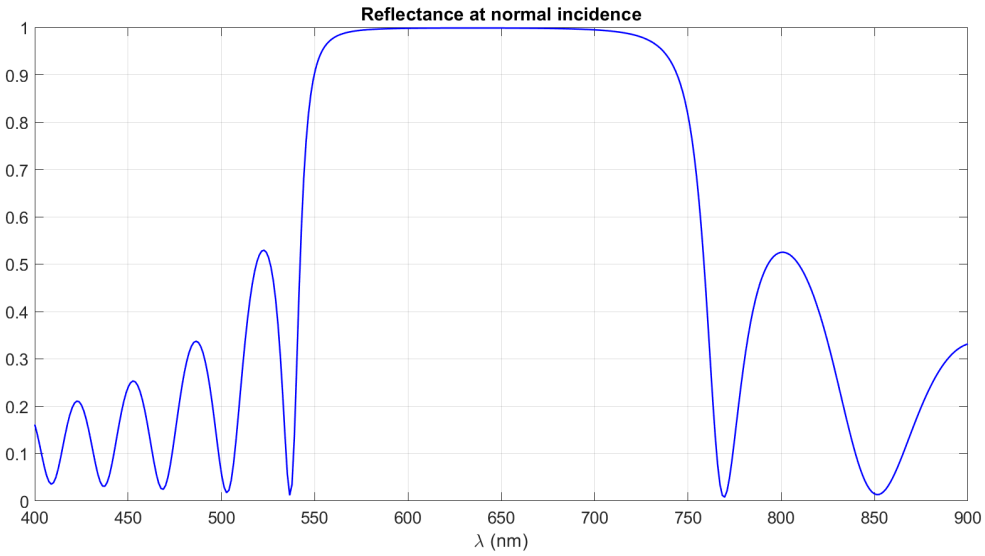

Figure 2.4: Reflectivity of a DBR made of alternating layers of $Nb_2O_5 - SiO_2$ with respective thicknesses of 67 nm and 108 nm. As we can see, the stop band is centered approximately around 640 nm. Calculated by means of RETICOLO.[3]

A higher refractive index contrast results in a broader stop band and higher reflectivity for the same number of periods.
It's important to point out that a DBR can be created also as a periodic corrugation on the surface of a sample [6], effectively behaving as a diffraction grating.

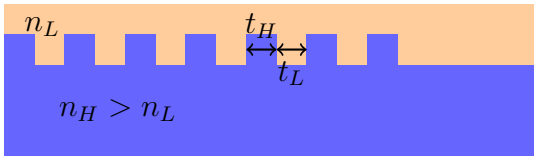

Figure 2.5: Diffraction grating.

The interaction between a surface mode with wavevector k_s (see section 2.3) and the DBR is described by the Bragg's law 2.24 for periodic objects, which associates a wavevector $K_g = \frac{2\pi}{\Lambda_g}$ to the grating, where $\Lambda_g = t_L + t_H$ is the DBR's period.

$$k_{//}^{diff} = k_{//}^{in} + mK_g \tag{2.24}$$

$k_{//}^{in}$ is the tangential component of the incident wavevector, that in our case corresponds to the whole k_s, since a surface mode doesn't have any orthogonal component, while $k_{//}^{diff}$ is the tangential component of the diffracted wavevector at the m^{th} diffraction order. If we want to exploit the surface mode, we can engineer the DBR so that $k_{//}^{diff} = 0$ for the first order ($m = \pm 1$), meaning that now the diffracted light is orthogonal to the surface, and can therefore be collected by a spectrometer and analyzed.

2.3 Surface modes

Surface modes are electromagnetic states confined at the interface between a photonic crystal and a different medium, such as air or a homogeneous dielectric. They arise when the periodic structure of the crystal is truncated, creating a break in translational symmetry that supports localized states within the forbidden band. Unlike bulk modes, which propagate inside the photonic crystal, surface modes decay evanescently into both adjoining materials, ensuring strong field confinement at the boundary.
The dispersion relation of surface modes lies within the forbidden band of the bulk crystal, meaning that their frequencies aren't allowed for propagating modes in the periodic medium. This property enables applications in sensing, light guiding, and enhancing light–matter interaction, as the high field localization can significantly increase the interaction strength with emitters. By engineering the surface termination, it is possible to tailor the dispersion and confinement of these modes.
In the two following subsections we will focus on two types of surface modes: **Tamm plasmons** and **Bloch surface waves**.

2.3.1 Tamm Plasmons

Tamm plasmons (TPs) aren't proper electromagnetic surface modes, they're better described as **localized interface states**, since they emerge at the boundary between a metal and a dielectric Bragg mirror.[4] Drawing a direct analogy to the electronic Tamm states predicted at crystal surfaces, TPs arise from the dual confinement provided by the negative permittivity of the metal on one side and the forbidden band of the Bragg reflector on the other.
To better understand how a Tamm plasmon is created, consider a virtual interface inside the first uniform layer of the DBR, the one in contact with the metal, and suppose the existence of an electromagnetic mode near the boundary, characterized by a frequency that is below the plasma frequency of the metal and near the Bragg frequency ω_0. By applying the TMM to the virtual interface, one finds that the following condition must be satisfied to grant the existence of the TP [4]

$$r_{left} r_{right} = 1 \tag{2.25}$$

where r_{left} and r_{right} are the reflection coefficients for a wave impinging respectively from the left side and from the right one. In our case, $r_{left} = r_{metal}$ and $r_{right} = r_{DBR}$. Therefore, joining any two structures for which eq.2.25 is verified, will result in a Tamm plasmon.

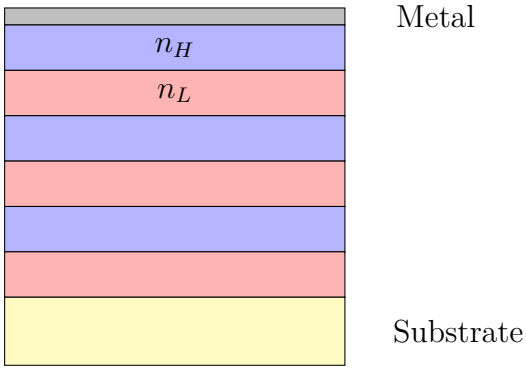

Figure 2.6: DBR with a thin metal layer on top.

Unlike conventional surface plasmon–polaritons, which reside outside the light cone and require complex coupling techniques such as prisms or gratings, Tamm plasmons lie within the light cone and can therefore be excited directly by normally incident light. Moreover, TPs exist for both transverse electric (TE) and transverse magnetic (TM) polarizations, with their dispersion lying inside the light cone. For small in-plane wavevectors $K \approx 0$, the dispersion relation is approximately parabolic,

$$\hbar\omega = \frac{\hbar^2 K^2}{2m^*}, \tag{2.26}$$

where m^* is an effective photon mass (on the order of $10^{-1}m_0$, with m_0 the free electron mass) and ω is the Tamm frequency. This property allows for straightforward optical access and spectral tunability by altering the Bragg mirror parameters.
Our sample's structure, starting from the bottom, is composed of: a glass substrate, 6 pairs of alternating niobium oxide (Nb_2O_5) and silicon oxide (SiO_2) of respective thicknesses 67 nm and 108 nm, one last 40 nm thick Nb_2O_5 layer, an 80 nm thick silver (Ag) layer, and finally a very thin (approximately between 5 and 10 nm) SiO_2 layer to prevent oxidation. The Tamm central wavelength is estimated to be around 620 nm, since as we can see in fig. 2.7 the parabola-like Tamm dispersion has its minimum in $\lambda_{TP} = 620nm$. Moreover, notice how the reflectivity increases as we get closer to $n_{eff} = n_1 sin(\theta_{in}) = \pm 1$, where n_1 is the air's refractive index and θ_{in} is the angle of incidence, proving that indeed the Tamm mode exists only within the light cone.

Numerical transfer-matrix simulations further show that the TP field decays exponentially into the metal (with a typical penetration depth of 10–30,nm) and into the Bragg mirror (hundreds of nanometers), forming a standing-wave pattern at the interface (see fig.2.8).

From an applications standpoint, Tamm plasmons offer:

- **Direct optical excitation:** Accessible with free-space light due to in-cone dispersion.

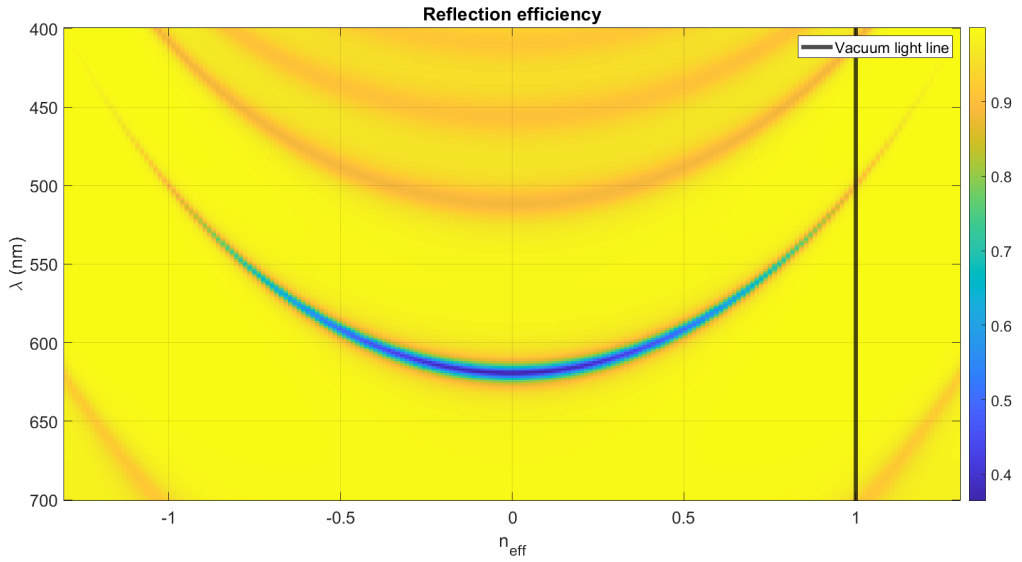

Figure 2.7: Reflectivity map of the Tamm structure in fig.2.6 at different vacuum wavelengths and effective refractive indexes, considering top planar incidence of a TE polarized planewave. Calculated by means of RETICOLO.[3]

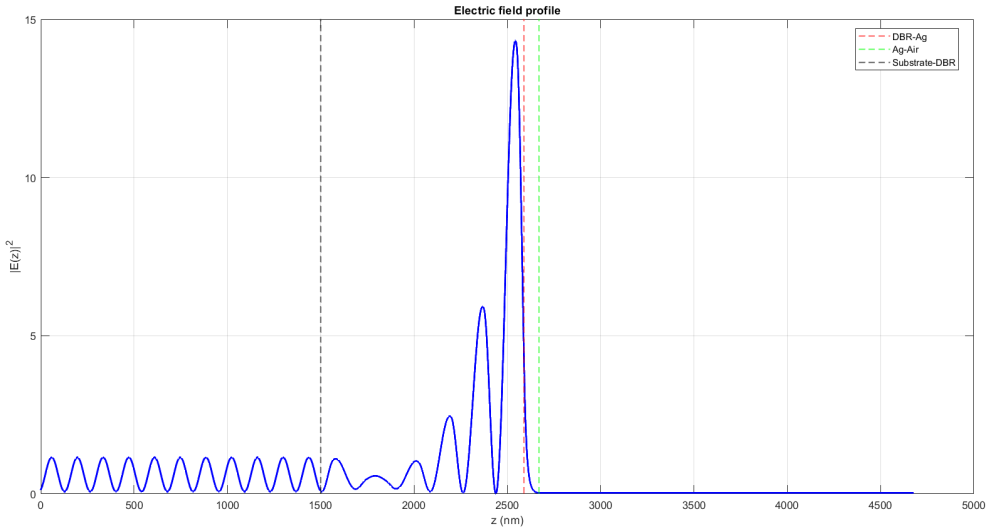

Figure 2.8: Electric field profile considering planar incidence of a TE polarized planewave at $\lambda_{TP} = 620nm$. Calculated by means of RETICOLO.[3]

- **Dual polarization:** Support for both TE and TM modes, unlike conventional surface plasmons which are TM-only.
- **Spectral tunability:** The resonance can be shifted across the forbidden band by varying the Bragg mirror's layer thicknesses or refractive-index contrast.
- **High quality factors:** Limited primarily by metal absorption and mirror leakage, with typical quality factor:

$$Q = \frac{\Re(\tilde{\omega})}{2\,\Im(\tilde{\omega})} \approx 200 - 300 \tag{2.27}$$

where $\tilde{\omega}$ is the eigenfrequency of TP, obtained by numerically solving 2.25, while $\Re(\tilde{\omega}) = \omega_{TP} = 2\pi\frac{c}{\lambda_{TP}}$ is the actual measurable frequency.

These features make Tamm plasmons attractive for a variety of nanophotonic applications, ranging from sensitive optical sensors to engineered light-matter interaction platforms.

2.3.2 Bloch Surface Waves

Bloch surface waves (BSW) refer to electromagnetic waves that are confined to the surface of a truncated periodic structure, such as a photonic crystal, where the structure ends at an interface with a homogeneous medium. Indeed, infinitely periodic structures can't exist, therefore a real-life PC becomes a dielectric multilayer stack with a finite number of periods. So, there will always be an interface interacting with the external medium. In a (real) 1DPC this gives rise to the so-called Bloch Surface Waves (BSWs), which are surface defects that manifest as dips in reflectivity inside the PBG. They're characterized by a field intensity confined in a narrow region near the surface and a long exponential decay tail that extends into the external medium, while the mode dispersion lies beyond the light cone, making it inaccessible from air.

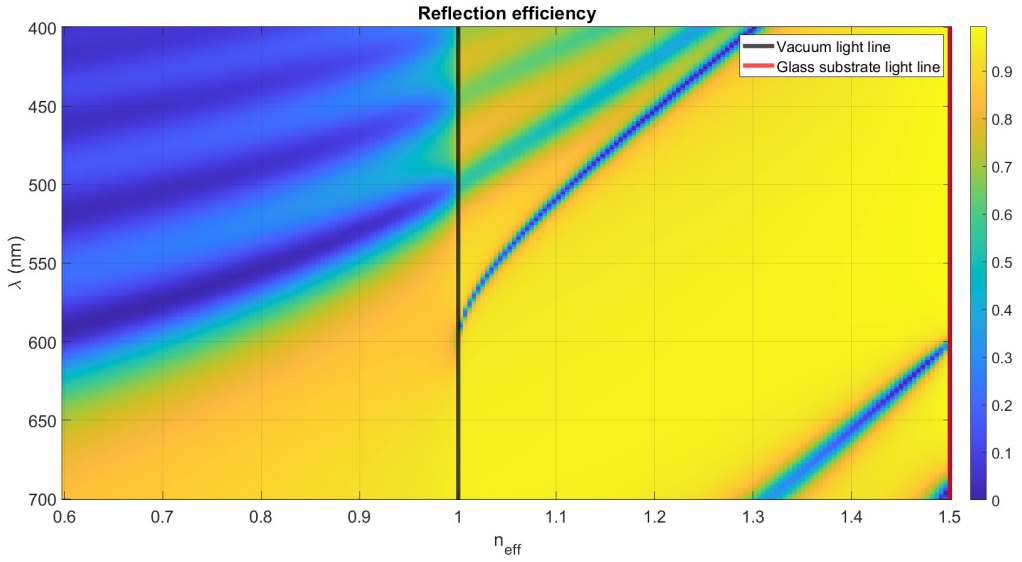

Figure 2.9: Reflectivity map of the SiO_2-Ta_2O_5 multilayer at different vacuum wavelengths and effective refractive indexes, considering a TE polarized planewave, impinging on the substrate side. Notice that $n_{eff} = n_{glass} sin(\theta_{in})$, where θ_{in} is the angle of incidence. Calculated by means of RETICOLO.[3]

The long exponential decay tail makes the BSWs sensitive to the optical properties of the surface, and therefore suitable for sensing applications and nanophotonic devices. As already mentioned, the BSW falls beyond the light cone, therefore it's not accessible from air (top incidence). However, if the multilayer is built upon a glass substrate ($n_{glass} \approx 1.5$), the BSW dispersion will lie inside the substrate's light cone, making it accessible from the bottom, as we can see in fig. 2.9. That's the reason why, on this type of structure, the properly matched radiation must impinge from the substrate side, so bottom incidence is required. Even in this way, if we're considering an ideal loss-less material, we wouldn't be able to see the BSW in the reflectivity map, since it can't be transmitted in air. In fact, when dealing with a real material, we must take into account

the loss due to absorption, represented by the imaginary part of the material's refractive index, which allows us to detect the BSW mode's missing fraction.
In other words, when a radiation that matches the momentum and energy of the BSW, impinges on the multilayer from the substrate side, it will travel up to the last layer/air interface and then it will undergo total internal reflection. As a consequence, a significant amount of energy is lost due to absorption, which appears as a dip in reflectivity.
Our sample is a dielectric multilayer stack composed of (from bottom to top): a glass substrate, 5 pairs of alternating silicon dioxide SiO_2 (low index) and tantalum oxide Ta_2O_5 (high index) with respective thicknesses of 137 nm and 95 nm, and one last 127 nm thick SiO_2 layer. So, the total thickness is estimated to be around 1.287 μm, making it a very thin and fragile sample. Unfortunately, it can't be any thicker, since our dielectric multilayer is made of *low leakage* materials, which would completely destroy the BSW, if it were to propagate through a longer path.

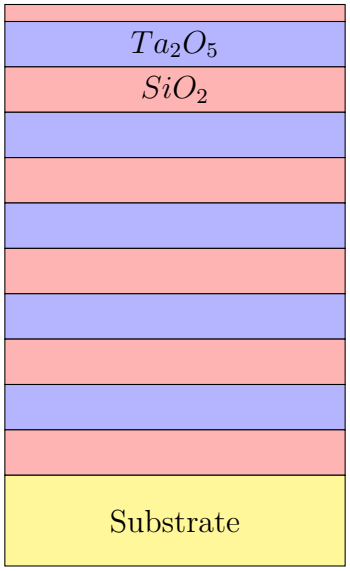

Figure 2.10: Dielectric multilayer stack.

To recover the BSW, which is trapped inside the sample, we need to couple it to a surface grating, like the one in fig. 2.5, such that $K_g = \frac{2\pi}{\Lambda_g} = n_{eff}\frac{2\pi}{\lambda_{BSW}} = k_{BSW}$. In this way we obtain $k_{//}^{diff} = 0$, according to eq. 2.24, if we're considering normal incidence ($k_{//}^{in} = 0$). By inverting the previous equation, we find that the grating period can be estimated with the following formula:

$$\Lambda_g = \frac{\lambda_{BSW}}{n_{eff}} \tag{2.28}$$

The BSW should couple to the grating in a wavelength range that goes from about 550 nm to 600 nm, because we know from previous literature [6] that the range in which hBN flakes usually emit is 570 nm - 640 nm. Thanks to the grating, the BSW is redirected

orthogonally to the sample's surface, therefore it can be collected and analyzed by a spectrometer. The information about λ_{BSW} and n_{eff} can be extracted from the reflectivity map in fig. 2.9, obtained by simulation.
Such grating can be created by means of a nanofabrication process called **Electron Beam Lithography** (EBL), which is explained in sec. 4.1. In the pictures below we can see how the surface's sample in fig. 2.10 looks like after performing a negative EBL.

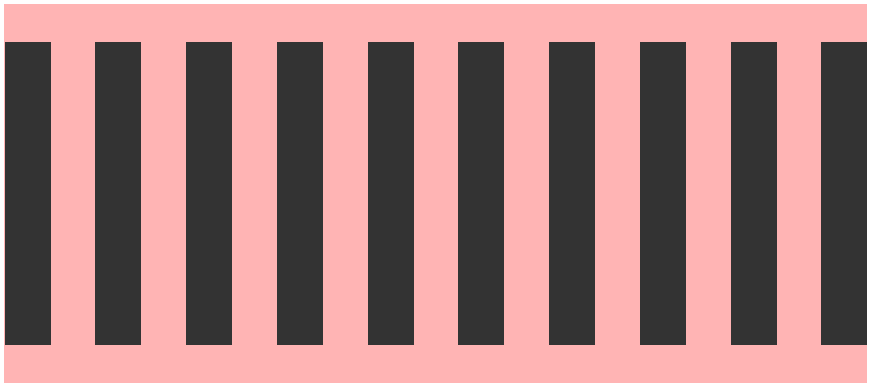

Figure 2.11: Top view after the development step. The black stripes are made of the negative resist ma-N 2401, while the pink background is the last SiO_2 layer of our sample.

Figure 2.12: Front view.

Chapter 3

Methodology

The main tool used to simulate the interaction between the dielectric multilayer and the TE polarized light is a software that operates under a MATLAB environment, called RETICOLO [3]. It computes the diffraction efficiencies and the diffracted amplitudes of gratings composed of stacks of lamellar structures. It incorporates routines for the calculation and visualisation of the electromagnetic fields inside and outside the grating. In brief, RETICOLO implements a frequency-domain modal method, known as the Rigorous Coupled Wave Analysis (RCWA).

3.1 Rigorous Coupled-Wave Analysis (RCWA)

Rigorous Coupled-Wave Analysis (RCWA) [8] is a semi-analytical method for solving Maxwell's equations in periodic dielectric structures. It is widely used to model and simulate the diffraction of electromagnetic waves by gratings, including surface-relief and volume holographic structures. RCWA can be viewed as a generalization of (Transfer Matrix Method) TMM, since when the periodic structure degenerates to a stack of homogeneous layers with no lateral periodicity, RCWA reduces to TMM. Moreover, both use a matrix formalism to connect fields across interfaces, but RCWA includes Fourier-mode coupling, while TMM only treats the fundamental mode.

3.1.1 Fourier Expansion of Permittivity

In RCWA, the periodic relative permittivity $\varepsilon_r(x)$ of the grating region is expanded as a Fourier series:

$$\varepsilon_r(x) = \sum_{h=-\infty}^{\infty} \varepsilon_h e^{j\frac{2\pi h x}{\Lambda_g}}, \tag{3.1}$$

where Λ_g is the grating period and ε_h are the Fourier coefficients.

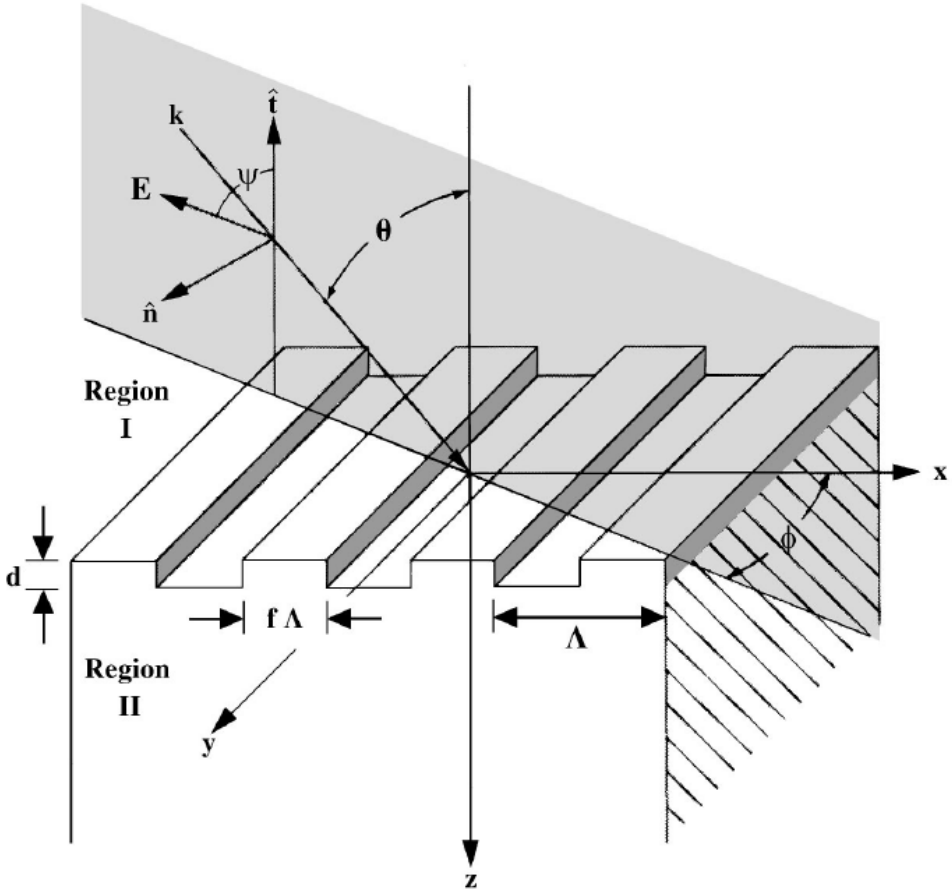

Figure 3.1: Rectangular diffraction grating with top-incidence.[8]

For binary gratings with fill factor f, ridge index n_r, and groove index n_g, the coefficients are given analytically as:

$$\varepsilon_0 = n_r^2 f + n_g^2(1-f) \tag{3.2}$$

$$\varepsilon_h = \frac{(n_r^2 - n_g^2)\sin(\pi h f)}{\pi h}, \quad h \neq 0 \tag{3.3}$$

3.1.2 Field Expansion and Matrix Formulation

The electric and magnetic fields inside the grating are expanded into spatial harmonics, considering TE polarization and planar incidence ($\phi = 0$):

$$E_y(x,z) = \sum_i S_i(z) e^{-jk_{x,i}x} \tag{3.4}$$

$$H_x(x,z) = \sum_i U_i(z) e^{-jk_{x,i}x} \tag{3.5}$$

where $k_{x,i}$ are the transverse wavevectors determined by the Floquet condition:

$$k_{x,i} = k_0 n_I \sin\theta - \frac{2\pi i}{\Lambda_g}, \tag{3.6}$$

with $k_0 = 2\pi/\lambda_0$ and λ_0 being the free-space wavelength.

By substituting eq.3.4 and 3.5 in the third and fourth Maxwell's equation, in the grating region we obtain a $2n \times 2n$ coupled differential equation system, where n is the number of Fourier harmonics retained in the field expansion. However, it can be reduced to a $n \times n$ system:

$$\frac{d^2\mathbf{S}(z)}{dz^2} = \mathbf{A}\mathbf{S}(z), \tag{3.7}$$

where the matrix $\mathbf{A}$ is defined as:

$$\mathbf{A} = \mathbf{K}_x^2 - \mathbf{E}, \tag{3.8}$$

with $\mathbf{K}_x$ a diagonal matrix of $k_{x,i}/k_0$ and $\mathbf{E}$ a Toeplitz matrix constructed from the ε_h coefficients.

3.1.3 Eigenmode Solution and Boundary Matching

The solution to the differential equation involves computing the eigenvalues and eigenvectors of $\mathbf{A}$:

$$\mathbf{S}(z) = \sum_m w_m \left(c_m^+ e^{-k_0 q_m z} + c_m^- e^{k_0 q_m (z-d)} \right), \tag{3.9}$$

where q_m are the square roots of the eigenvalues and w_m are the corresponding eigenvectors. The coefficients $c_m^{\pm}$ are determined by matching boundary conditions for the tangential electric and magnetic fields at the interfaces $z = 0$ and $z = d$.

3.1.4 Diffraction Efficiencies and Stability

The diffraction efficiencies for the i^{th} order reflected and transmitted waves are given by:

$$DE_r^{(i)} = |R_i|^2 \cdot \mathrm{Re}\left(\frac{k_{I,z}^{(i)}}{k_0 n_I \cos\theta}\right) \tag{3.10}$$

$$DE_t^{(i)} = |T_i|^2 \cdot \mathrm{Re}\left(\frac{k_{II,z}^{(i)}}{k_0 n_I \cos\theta}\right) \tag{3.11}$$

RCWA is inherently stable when properly implemented. Potential numerical issues due to evanescent modes are avoided by normalizing exponential terms to ensure that they decay (i.e., arguments are always negative real).

The accuracy of RCWA depends on the number of Fourier harmonics retained in the

calculation. Deeper gratings, larger periods, TM polarization, and conical diffraction typically require more harmonics for convergence. Convergence is verified by monitoring the stability of diffraction efficiencies as the number of harmonics increases.

Chapter 4

Experimental methods

4.1 Electron Beam Lithography

Electron Beam Lithography (EBL) was used to fabricate gratings with different periods Λ_g ranging from 510 nm to 590 nm, according to eq. 2.28, to be sure that the grating wavevector matches the BSW and satisfy $k_{//}^{diff} = 0$. Actually, even if a perfect coupling isn't achieved, since we don't have much control over the resist's thickness, it wouldn't be an issue, we would just need to collect the emitted light along a different direction, i.e. different diffraction order.
The process was performed at the *Istituto Nazionale di Ricerca Metrologica (INRIM)* using a FEI Quanta 3D FEG Dual Beam system. It is a versatile instrument that combines a high-resolution field emission scanning electron microscope (FE-SEM) with a focused ion beam (FIB) column in a single platform. This configuration allows both imaging and site-specific material modification or removal at the nanoscale. The electron column provides high-resolution imaging capabilities with sub-nanometer resolution, while the ion column, typically employing a gallium ion source, enables precise milling, cross-sectioning, and deposition of materials. The Quanta 3D FEG supports multiple operating modes, including high-vacuum, low-vacuum, and environmental (ESEM) modes, making it suitable for the analysis of both conductive and non-conductive samples without extensive preparation.

EBL is a direct-write technique that allows the fabrication of nanostructures with extremely high resolution. The process consists of several key steps:

1. **Substrate preparation and resist coating in cleanroom:** The substrate is first cleaned to remove any surface contaminants. A thin film of electron-sensitive resist is then deposited, using spin-coating to ensure a uniform thickness. A soft bake is typically performed to remove residual solvents and enhance the stability of the resist layer.

2. **Electron beam exposure:** The substrate is loaded into the FEI Quanta 3D FEG

Dual Beam system, where a finely focused electron beam is scanned across the resist according to a computer-defined pattern. The interaction of the electrons with the resist modifies its chemical structure: in positive resists chain scission occurs, while in negative resists cross-linking dominates. These changes alter the solubility of the resist in the subsequent development step, making it higher if positive and lower if negative.

3. **Development in cleanroom:** The sample is immersed in a chemical developer that selectively removes either the exposed or unexposed regions of the resist, depending on the resist type. This process reveals the patterned resist mask with nanoscale resolution.

4. **Pattern transfer (optional):** The resist pattern can then be used as a mask for material deposition (e.g., metal evaporation followed by lift-off) or for etching processes that transfer the pattern into the underlying layers. The choice of transfer method depends on the target structure and material system.

5. **Resist removal (optional):** If required, the remaining resist is stripped away, leaving behind the final nanostructure defined on the substrate.

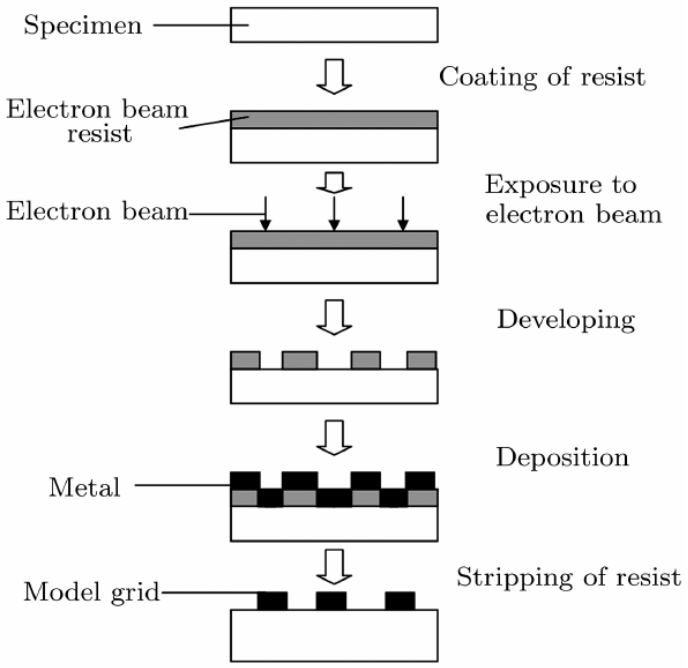

Figure 4.1: Schematic of EBL process with a positive resist. [5]

The process begins in a ISO Class-5 cleanroom, where a thin layer of the negative tone photoresist ma-N 2401 is spin coated at 6000 rpm for 40 seconds onto the sample surface, then it is baked at 100 °C for 4 minutes on a hot plate. In this way we can achieve a resist

layer with a thickness of less than 100 nm. Before starting the writing process, we set a SEM aperture of 20 μm, a spot of 4.0 and an AV (Accelerating Voltage) of 30 kV. Then, since our multilayer is highly insulating, we perform the EBL in low vacuum condition by injecting water vapour in the SEM chamber up to a final pressure of 0.8 mbar. A dose test was designed to ensure the correct dimension of the final structures, varying the deposited dose from 150% to 400% of 200 $\mu C/cm^2$. Finally, the sample is developed in cleanroom with ma-D 331 (NaOH water based solution) for 1 minute, and then washed with double distilled water for 30 seconds. As a last step, we look for the gratings using an optical microscope, we take some pictures, and repeat the process with the SEM, so that we can also measure the gratings' period and filling factor, and compare them with the original design.

Before performing EBL on our multilayer, we ran some tests on a simple SiO_2 sample to optimize as best as possible the different parameters, in particular the SEM aperture, the dose and the development time. The main differences between the test sample and our multilayer were the thickness and the conductivity, which allowed us to take the SEM pictures in high vacuum, when dealing with the test sample, ensuring a way better resolution.

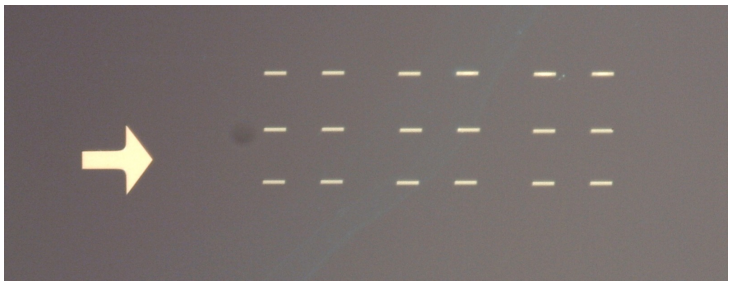

Figure 4.2: Optical microscope picture of the test gratings on the SiO_2 sample. The gratings, designed to have a 510 nm period, come in couples with a 20 μm distance between each other, and each couple of the 3x3 array is made using a different dose, which is lowest for the (3,1) element and increases linearly, up to the (1,3) element. The big arrow is just a marker to find the structures more easily.

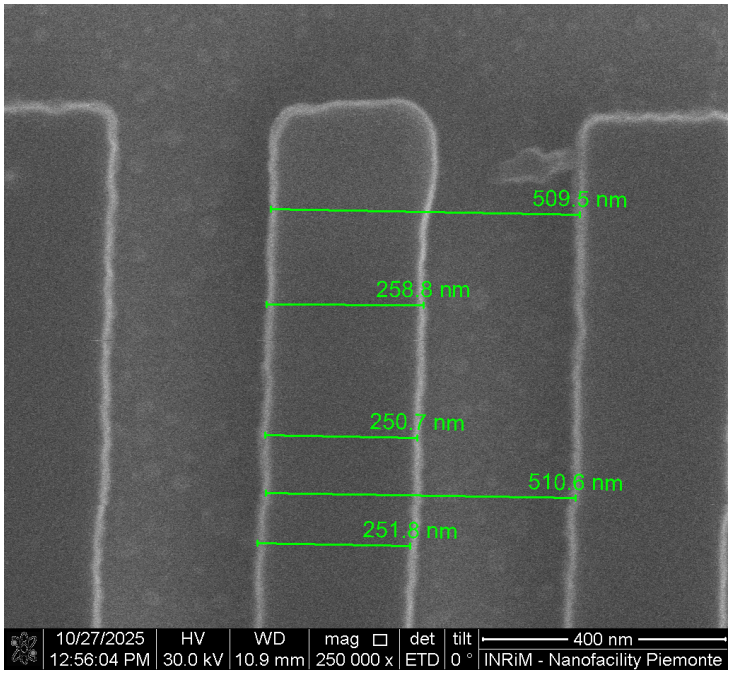

Figure 4.3: SEM picture of the 510 nm test gratings on the SiO_2 sample in high vacuum.

Each grating was designed to have 25 periods, ranging from 510 nm to 590 nm, a filling factor of 0.5 and a vertical length of 2 μm. The actual gratings approximately respect the given periods, with variations of the order of 10 nm, while the filling factor changes noticeably across the different elements of the array, depending on the dose. Following this criteria, we can conclude that the best gratings are the ones in position (3,1) and (3,2), which correspond respectively to the 150% and 181.3% doses.

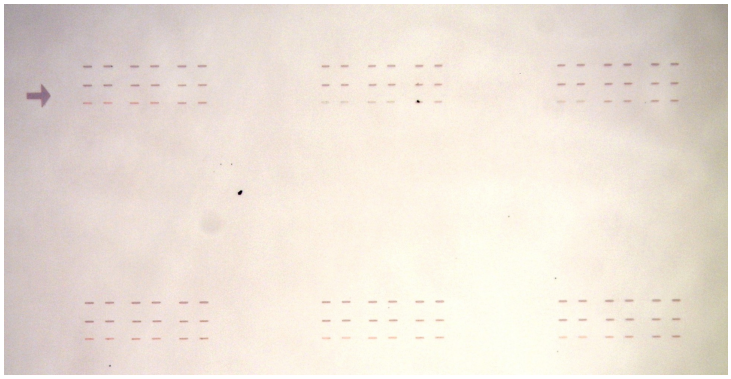

(a) Optical microscope picture of all the gratings on our multilayer.

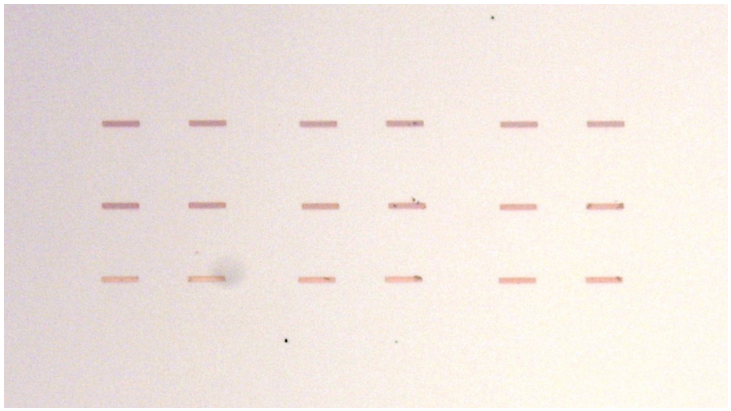

(b) Close up picture of one grating. As we can see, the same dose test was performed, creating a 3x3 array.

Starting from position (1,2) and going clockwise we have the following periods: 510 nm, 530 nm, 550 nm, 570 nm and 590 nm in (2,1). The grating in position (1,1) was designed to have a 490 nm period, but by mistake the 590 nm was replicated.

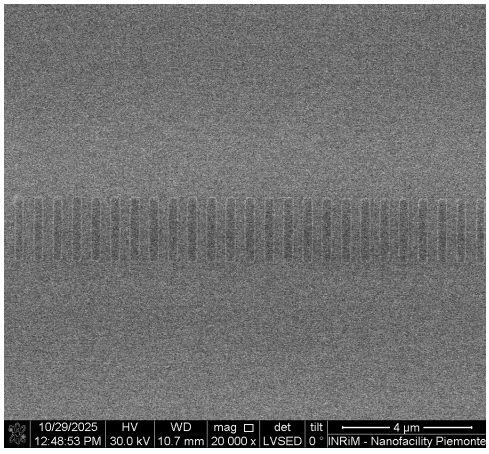

(a) SEM picture in low vacuum of the 590 nm grating.

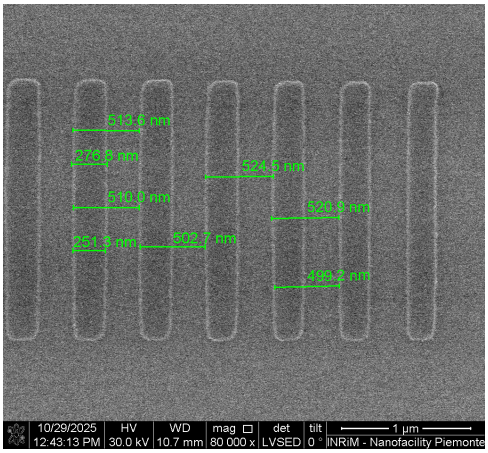

(b) SEM picture in low vacuum of the 510 nm grating. Both the period of 510 nm and the stripes' thickness of 255 nm are approximately respected.

Notice that, with every additional layer (including the hBN flakes themselves), the

BSW dispersion is shifted towards longer wavelengths. In fig. 4.6, for example, we can see how the dispersion differs from the one in fig. 2.9 after adding a 75 nm thick layer of resist. This effect is called **dielectric loading**. Unfortunately, we can't control in a fine way the resist's thickness during the spin coating phase, therefore it was not possible to make a more precise estimate of the grating's period to ensure perfect coupling to the BSW. However, we know from the ma-N 2401 datasheet that a spin coating at 6000 rpm results in a less than 100 nm thickness.

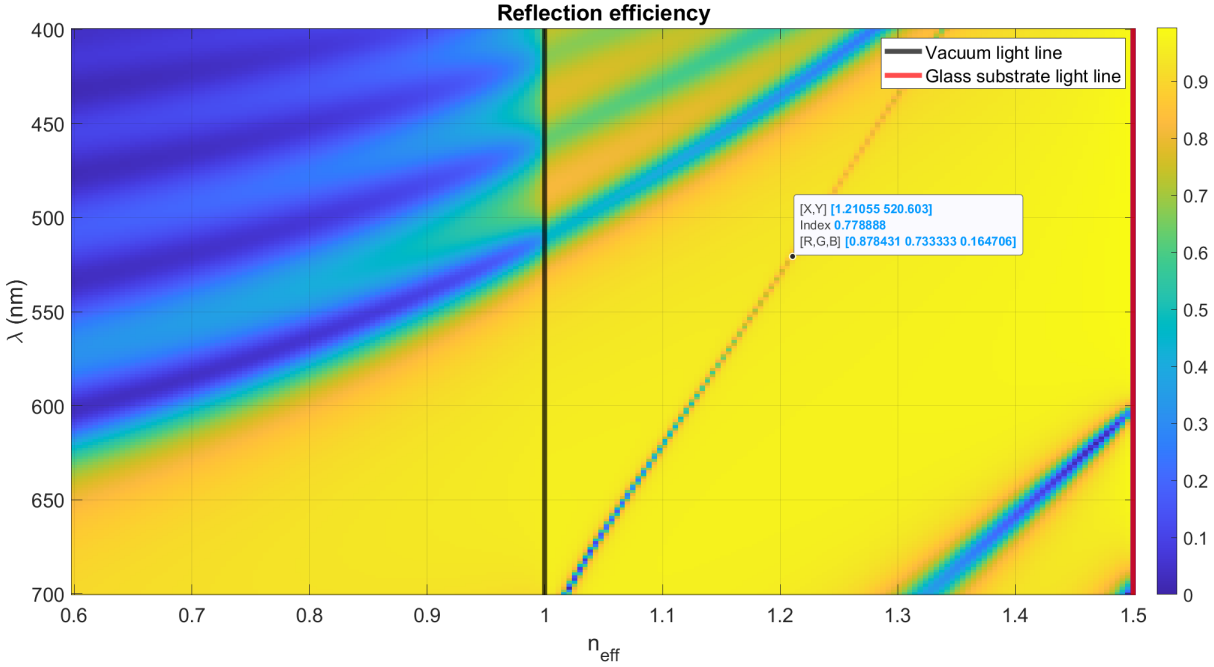

Figure 4.6: Reflectivity map of the multilayer topped with a resist layer. Calculated by means of RETICOLO [3].

After the development step, the sample's surface refractive index profile is expected to behave as in fig. 4.7.

Then, to test whether the grating works, we can make another simulation, before actual optical measurements, including such grating in the structure's design, but considering ideal lossless materials. As mentioned in sec. 2.3.2, the BSW can't propagate in air/vacuum, therefore it wouldn't be visible in the reflectivity map of an ideal material, unless there's a surface grating that matches the BSW momentum.

As we can see in fig.4.8, now the BSW is visible even in an ideal lossless material, despite laying beyond the light cone. To further test the grating's working principle, we consider also the diffraction efficiency in **top incidence**, and therefore we reduce our visibility field to the light cone. The two BSWs appear as light blue lines, crossing each other at $n_{eff} = 0$ (normal incidence); the BSW dispersion now lies in a passing band, but it looks brighter than the background, since part of it couples and decouples to the grating, and comes back at the same angle of incidence. That's the reason why

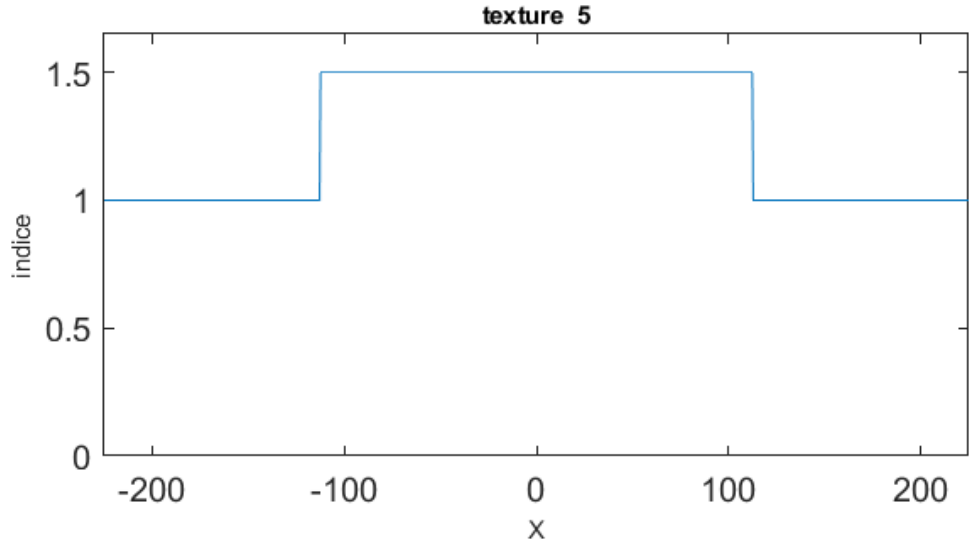

Figure 4.7: Refractive index profile along x of texture 5, e.g. the last layer of our structure. The plot shows just one period, but RETICOLO automatically replicates it to simulate a periodic infinite structure. Computed by means of RETICOLO [3].

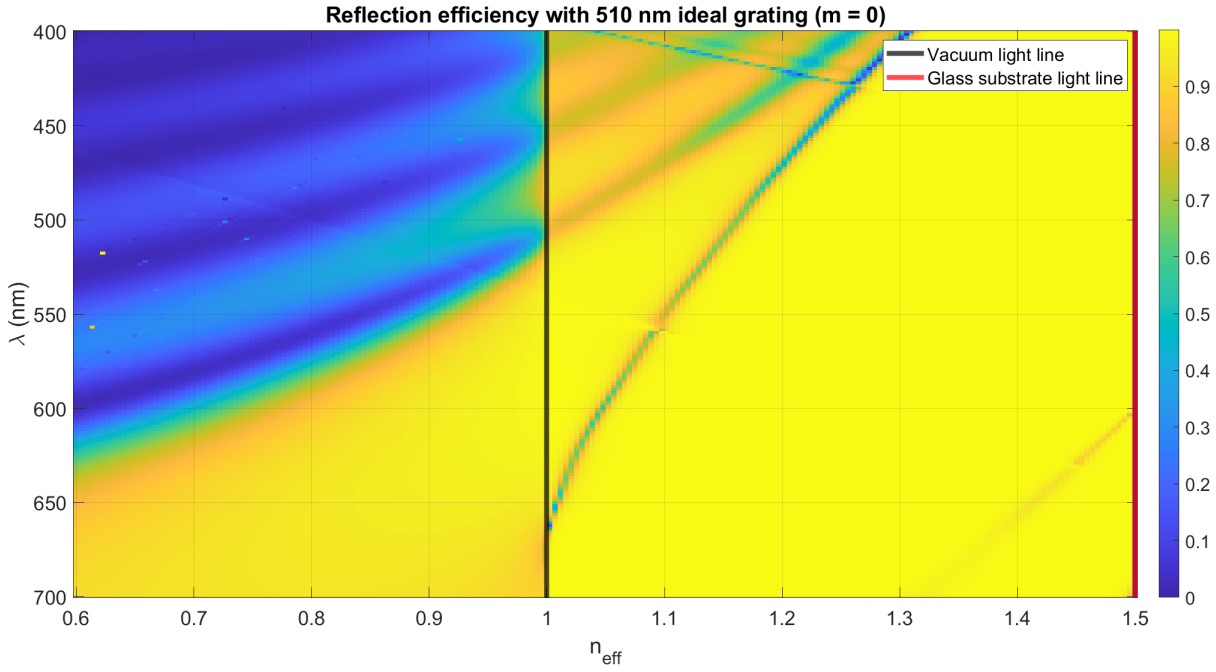

Figure 4.8: Reflection efficiency of an ideal multilayer with **bottom illumination**. Calculated by means of RETICOLO [3].

the BSW is visible at order $m = 0$, although it's not reflected, but diffracted. This shows that the grating works properly, since in absence of coupling, the BSW would propagate undisturbed along the surface, and we would never be able to see it in a reflectivity map.

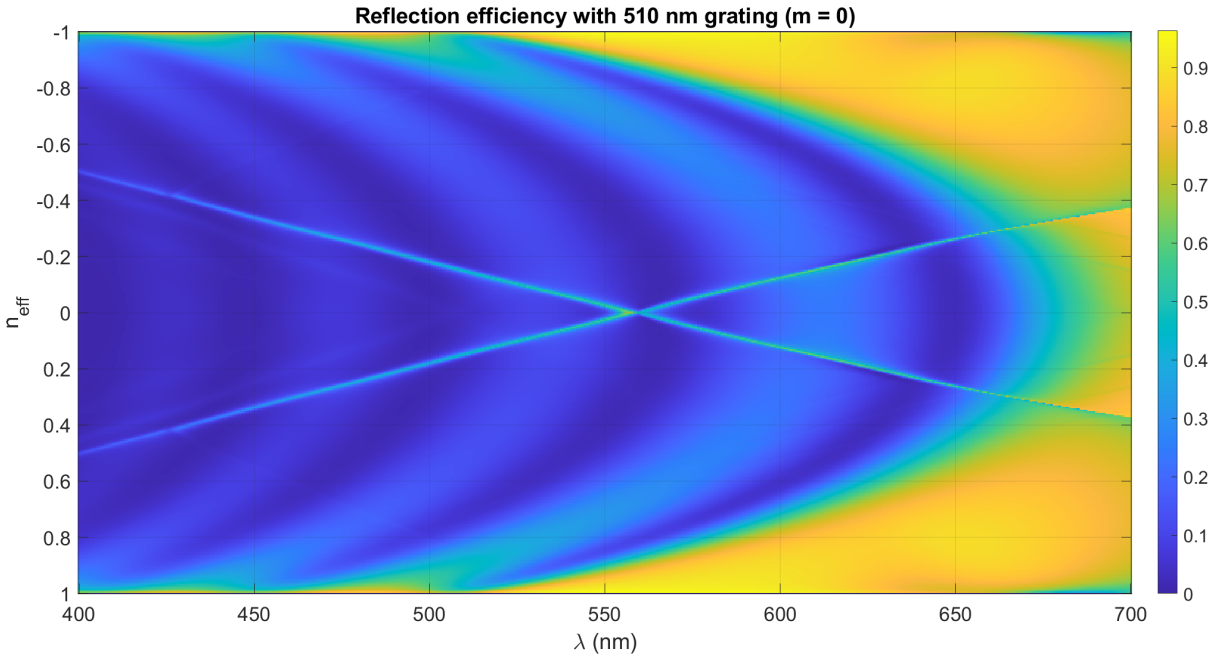

Figure 4.9: Reflection efficiency with **top illumination**. The axes are now swapped with respect to the previous simulations, to allow an easier comparison with the experimental measurements in the next sections. Calculated by means of RETICOLO [3].

Now, let's switch back to **bottom illumination** and expand the angle of incidence range, $-1.5 \leq n_{eff} \leq 1.5$. Remember that $n_{eff} = n_{glass} sin(\theta_{in})$, where $n_{glass} \approx 1.5$ and θ_{in} is the angle of incidence. Thanks to the greater range we can observe both the **directly coupled** BSW, which is visible just due to absorption by the real multilayer, and the **grating-coupled** BSW, which is diffracted by the grating on top of the multilayer.

More in detail, at diffraction order $m = 0$ in fig. 4.10, i.e. in reflection, we can see the directly coupled BSW (marked by the blue arrows), which is outside the light cone, appears as a reflectivity dip, and is visible also when there is no grating (see fig. 4.11); moreover, the grating-coupled, and therefore diffracted, BSW is there too (marked by red arrows), which instead manifests as a reflectivity peak inside the light cone across a propagating frequency range.

Since no light is diffracted in the 'no grating' case, of course, we report here just the reflection efficiency at $m = 0$ order in fig. 4.11. Then, in fig. 4.13 and 4.12 we can analyze the diffraction efficiencies respectively of order $m = -1$ and $m = 1$ when there's a 510 nm grating; the two maps appear to be mirrored, since the incident light comes from both positive and negative angles. Once again, we can see the grating-coupled (red arrow) and directly coupled (blue arrow) BSWs, but now they are both equally bright. This is due to the fact that actually they both couple to the grating, but only the grating-coupled one is in resonance condition, while the directly coupled one simply highlights the existence of the BSW mode, regardless of the grating's presence. In a clearer way, the former actually needs to be supplied by the grating's momentum K_g in order to be

excited, while the latter would exist anyway, although of course it wouldn't get diffracted in absence of grating.

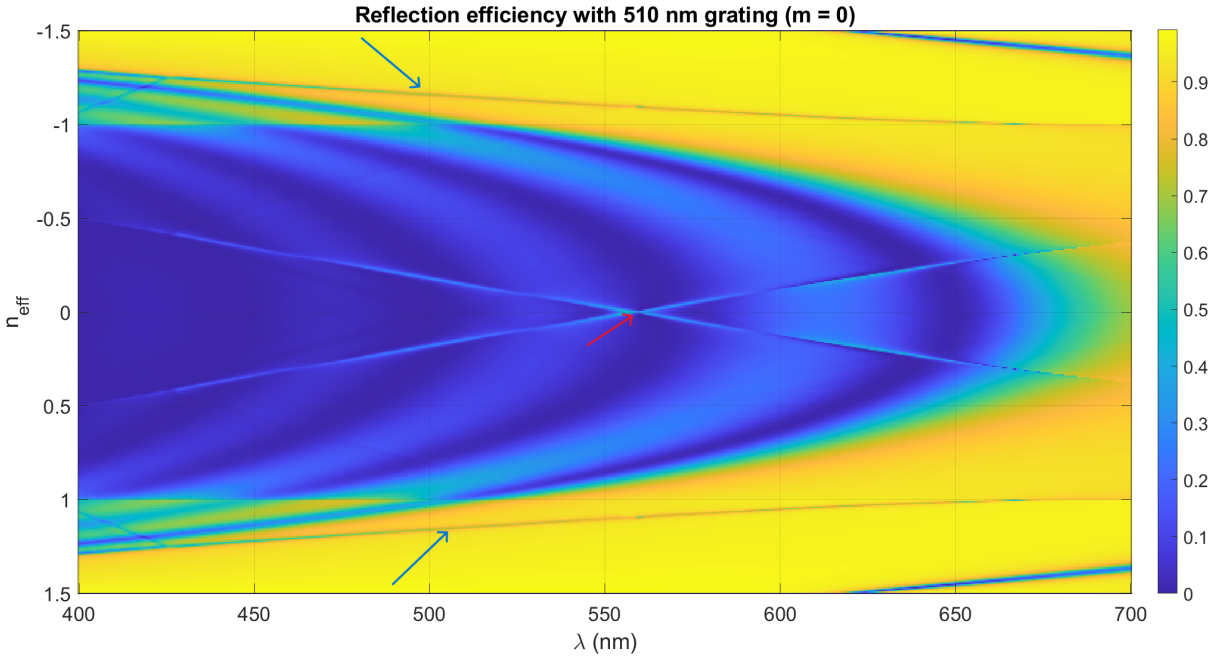

Figure 4.10: Reflection efficiency of a real multilayer topped by a 510 nm grating in **bottom illumination**. Calculated by means of RETICOLO [3]. The blue arrows mark the **directly coupled** BSW, while the red one highlights the **grating-coupled** BSW.

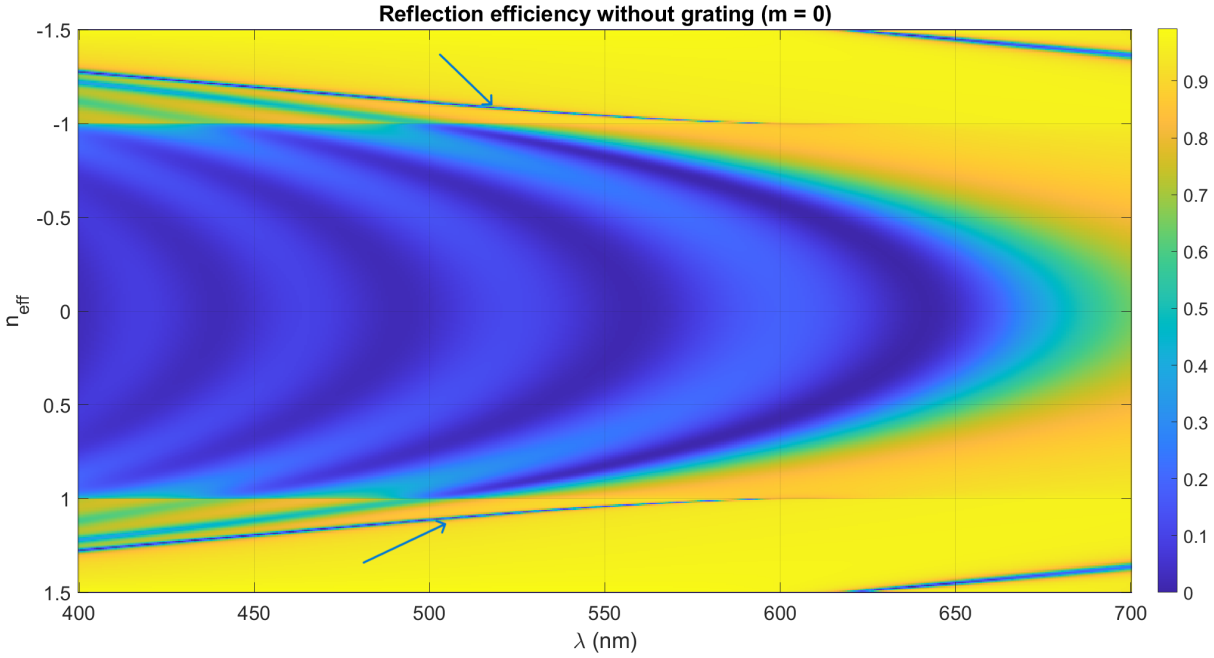

Figure 4.11: Reflection efficiency of a real multilayer without any grating in **bottom illumination**. Calculated by means of RETICOLO [3]. Here there are only the **directly coupled** BSWs, marked by blue arrows.

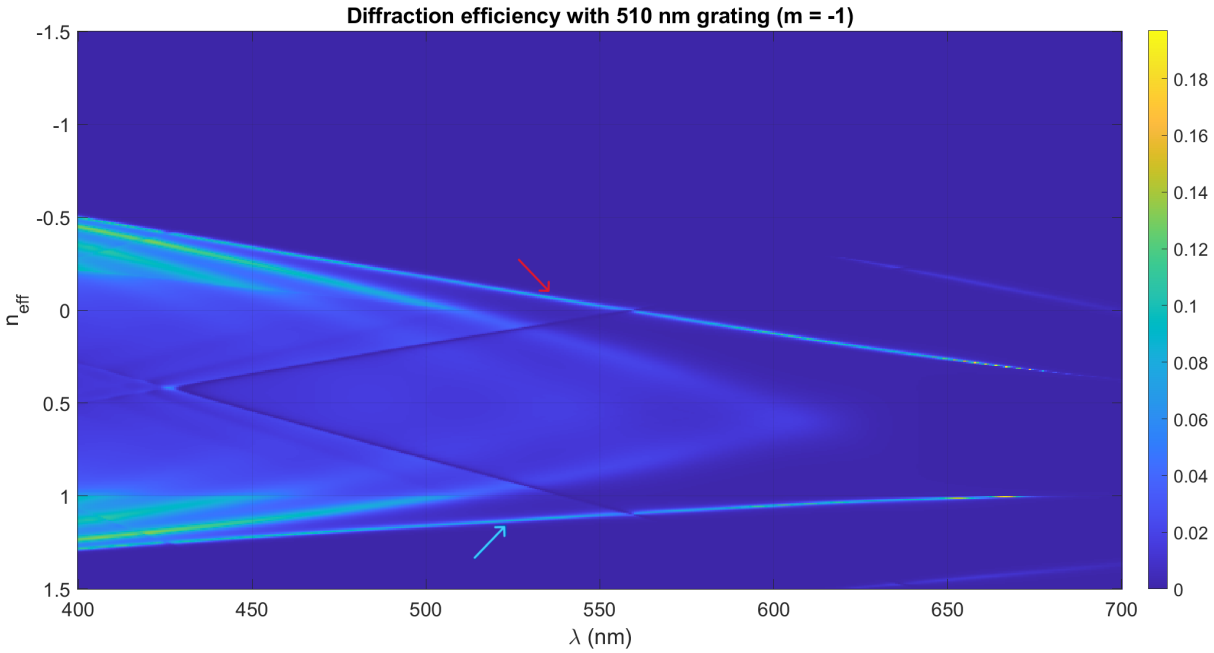

Figure 4.12: Diffraction efficiency at $m = -1$ order of a real multilayer with **bottom illumination**. Calculated by means of RETICOLO [3]. The blue arrow marks the **directly coupled** BSW, while the red one highlights the **grating-coupled** BSW.

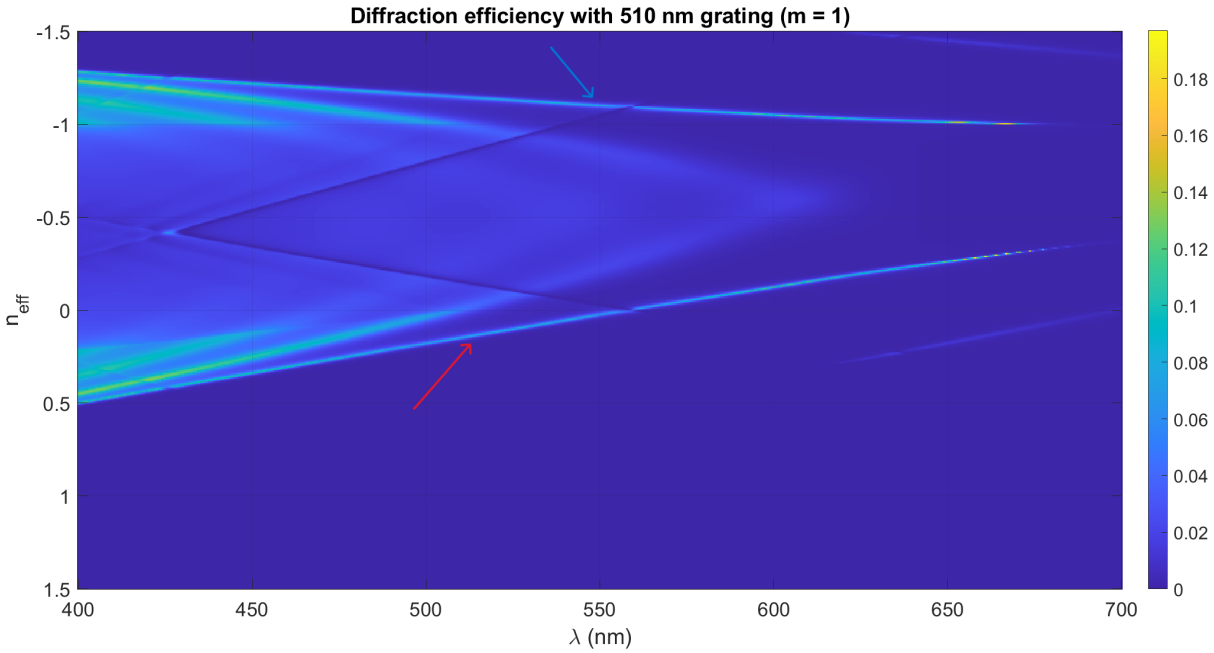

Figure 4.13: Diffraction efficiency at $m = 1$ order of a real multilayer with **bottom illumination**. Calculated by means of RETICOLO [3].

4.2 Hexagonal boron nitride

Hexagonal boron nitride (hBN) consists of alternating boron and nitrogen atoms arranged in a honeycomb lattice, much like graphene.[6] Thanks to its wide band gap, it excels as an electronic and photonic material, offering thermal stability and electrical insulation. Common fabrication methods include chemical vapor deposition (CVD) and high-pressure, high-temperature (HPHT) synthesis. While CVD-grown hBN can be formed directly on target devices, HPHT-produced crystals require transfer steps but yield the highest crystal quality.
Over the past ten years, hBN has emerged as a promising host for quantum light sources, because of their photostability, tunability, high-purity emission, robustness and high brightness at room temperature [7]. Although the precise mechanisms remain under investigation, these single-photon emitters are generally linked to lattice imperfections, most often nitrogen vacancies or the incorporation of foreign atoms like carbon. These defects introduce discrete energy levels within the band gap, where charge carriers can become trapped and then recombine, emitting photons. To reliably produce such emitters, one must either engineer specific defects or activate latent ones. Unlike transition-metal dichalcogenides, whose emitters typically depend on excitonic states in few-layer films, hBN defects function across a broad range of thicknesses and can operate as quantum emitters at room temperature.

4.2.1 Peeling

The first step is to create flakes, starting from a HPHT-synthesized hBN crystal, through a process called **peeling** or **exfoliation**, described in the following.
A hBN bulky crystal is placed on a piece of strong adhesive PDMS tape, which is then closed on itself several times, as the crystal decomposes into thin shiny scraps, which are the flakes.
Then, a little piece of another weaker PDMS tape, namely Gelfilm by Gel-pak, is cut and, after removing the protective thin layer, its sticky side is brought into contact with the flakes on the tape. After this, the piece of PDMS is fixed by means of a double face 3M tape to a cantilever, which is then used also to fix the multilayer to the sample holder of an optical microscope.

The cantilever can be moved in all 3 directions, so it's taken under the objective of the optical microscope, in order to check how the flakes appear. Ideally, we would like to transfer a thin large flake, so one that appears light blue and almost transparent.

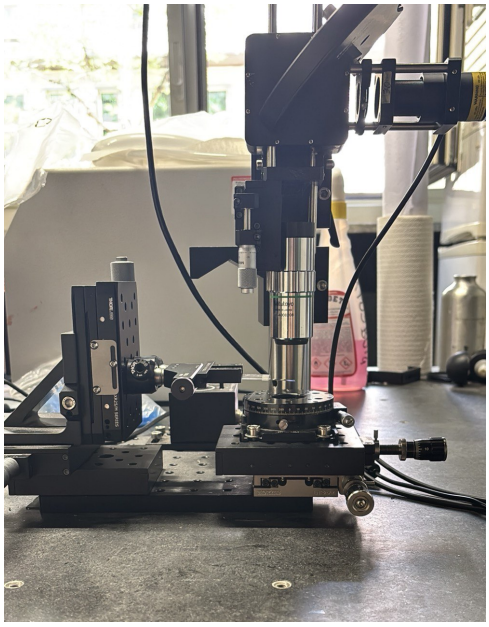

(a) Experimental setup. It's the same used in [6].

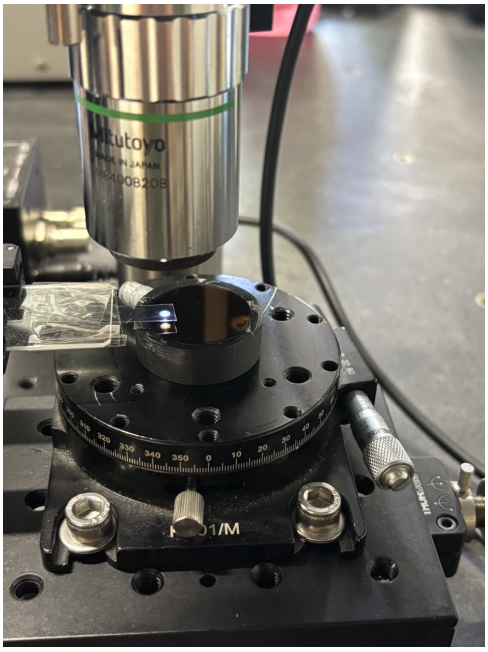

(b) Close up of the PDMS piece fixed to the cantilever and the multilayer sample.

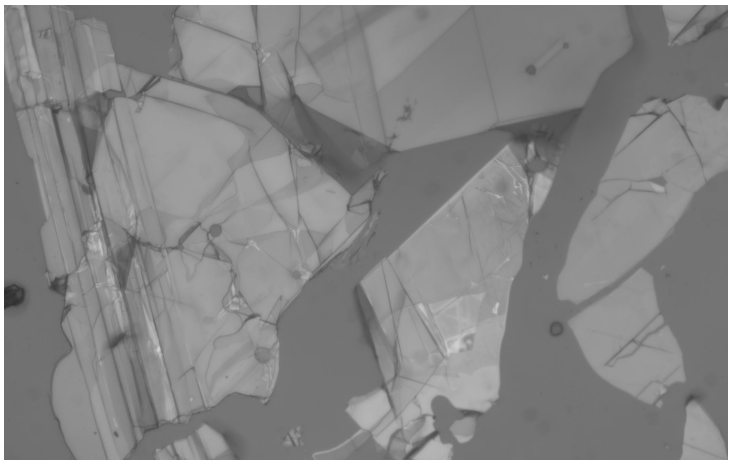

Figure 4.15: A large and thick flake with many cracks, not a suitable one.

4.2.2 Flake transfer

There are several techniques to transfer hBN flakes from a surface to another one [7], such as wet transfer, dry transfer, semi-dry transfer, direct growth, inorganic membrane-assisted transfer, adhesive layer transfer etc. Each of them carries its own issues, for example polymers and solvents can introduce optically active defects, such as trapped bubbles, water and residues that reduce the quality of the emitters. Hence, simplifying the transfer process by minimizing chemical involvement is crucial.
We adopted a dry transfer method, where the flake on the PDMS tape is brought into contact with the sample's surface, by lowering the cantilever. It's possible to understand that contact has been reached, because the flake's color changes. Then, the most difficult

part of the transfer process follows: detachment. It must be as slow as possible, ideally one should be able to monitor the adhesion front and watch it going around the flake, which implies that it's been detached from the PDMS tape.
However, dry transfer is a statistical process, many trials are required, therefore the successful transfer of a specific flake is very unlikely. It has been shown [7] that there are some parameters that can be optimized to increase the chances of success: temperature, contact time and stage velocity. However, the only one of interest regarding our transfer technique is **contact time**.
After several unsuccessful trials with a contact time of barely half minute, we decided to adopt a different approach. Basically, the piece of PDMS, one with many flakes attached, is left into contact with the multilayer's surface for about 24 hours; then, as slowly as possible, the cantilever is lifted, allowing some of the flakes to detach from the PDMS, thanks to the Van der Waals forces between them and the sample's surface.

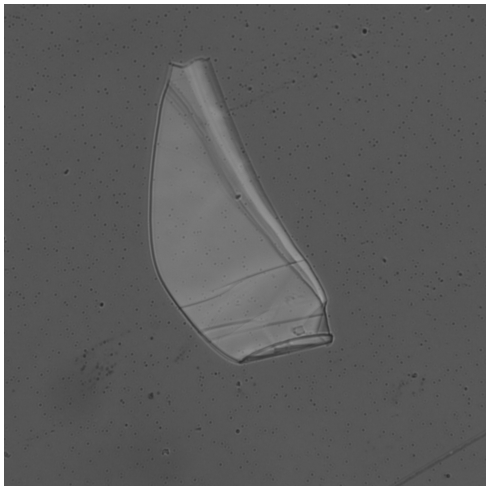

Figure 4.16: A nice flake transferred on the sample, but quite close to the border.

It's important to notice that the transfer technique we adopted eventually isn't the best one, because of the low efficiency and high probability of leaving PDMS residues on the sample. A better approach could be the one illustrated in [7], where an all-dry Temporary Transfer Stamp (TTS), made of a PDMS-PVC tape, is used to efficiently move the selected flake from one point to another on the sample's surface. The key point is that the PVC (polyvinyl chloride) film has a temperature-dependent adhesion, which can be exploited to increase the probabilities of a successful transfer. Furthermore, it has been shown that TTS method doesn't alter the photostability and emission purity of hBN-based SPSs.

4.2.3 Defects creation

Because of the adopted transfer method, most flakes already have some cracks, defects and non-uniform thickness, an example is reported in fig. 4.17. Therefore, if we shine

a laser on them, using the optical setup described in sec. 4.3, we can see luminescence coming from some point-like blinking spots, reported frame by frame in fig. 4.18.

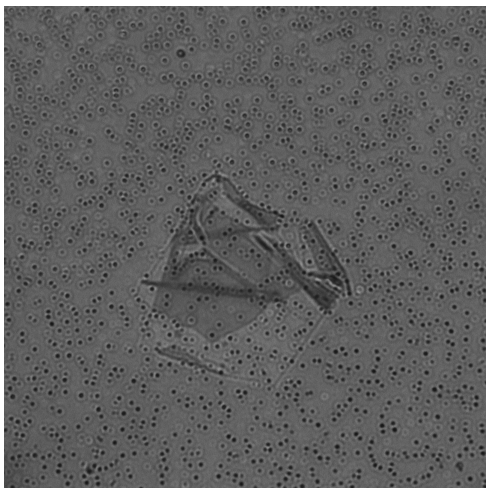

Figure 4.17: Flake with many defects, folds, and non-uniform thickness.

The luminescence coming from "natural" defects of the flake, or from impurities on the sample's surface, acts as background noise, and therefore makes it difficult to recognize and characterize the emission of possible single photon sources. This is the reason why it's preferable to artificially create some other point-like defects to be studied.
We know from previous studies [6] that point-like defects in hBN can be created by means of a **Focused Ion Beam** (FIB), exploiting a standard Gallium source. However, this technique carries the risk of being too disruptive, because if a too high dose is applied, we may end up with a hole, instead of a point-like defect. There's also another issue to be taken into account: deposition of carbon residuals at the exposed sites. They're due to the interaction between contaminants inside the microscope vacuum chamber and the charged particles of the sample, and unfortunately their fluoresce is in the same spectral region as the defect states, creating a background disturbance.
A better approach could be to employ a NanoFrazor thermal scanning-probe [2] lithography (t-SPL) system (Heidelberg Instruments Nano AG) to locally induce point defects in exfoliated hBN flakes.
The NanoFrazor integrates high-resolution thermal lithography with in-situ topographic imaging, enabling nanoscale modification and immediate inspection of the sample surface. It uses a resistively heated atomic-force microscopy (AFM) tip capable of reaching temperatures up to $\sim$ 1300 °C, with a set-point stability better than 1 K. The conical silicon tip, with a radius below 10 nm, allows for feature sizes down to approximately 15 nm laterally and vertical (depth) control with a precision of about 2 nm. The writing process is thermally activated: local heating of the tip causes sublimation or thermal decomposition of the target material, depending on its composition and the applied contact force. The system is also equipped with a direct laser sublimation (DLS) module

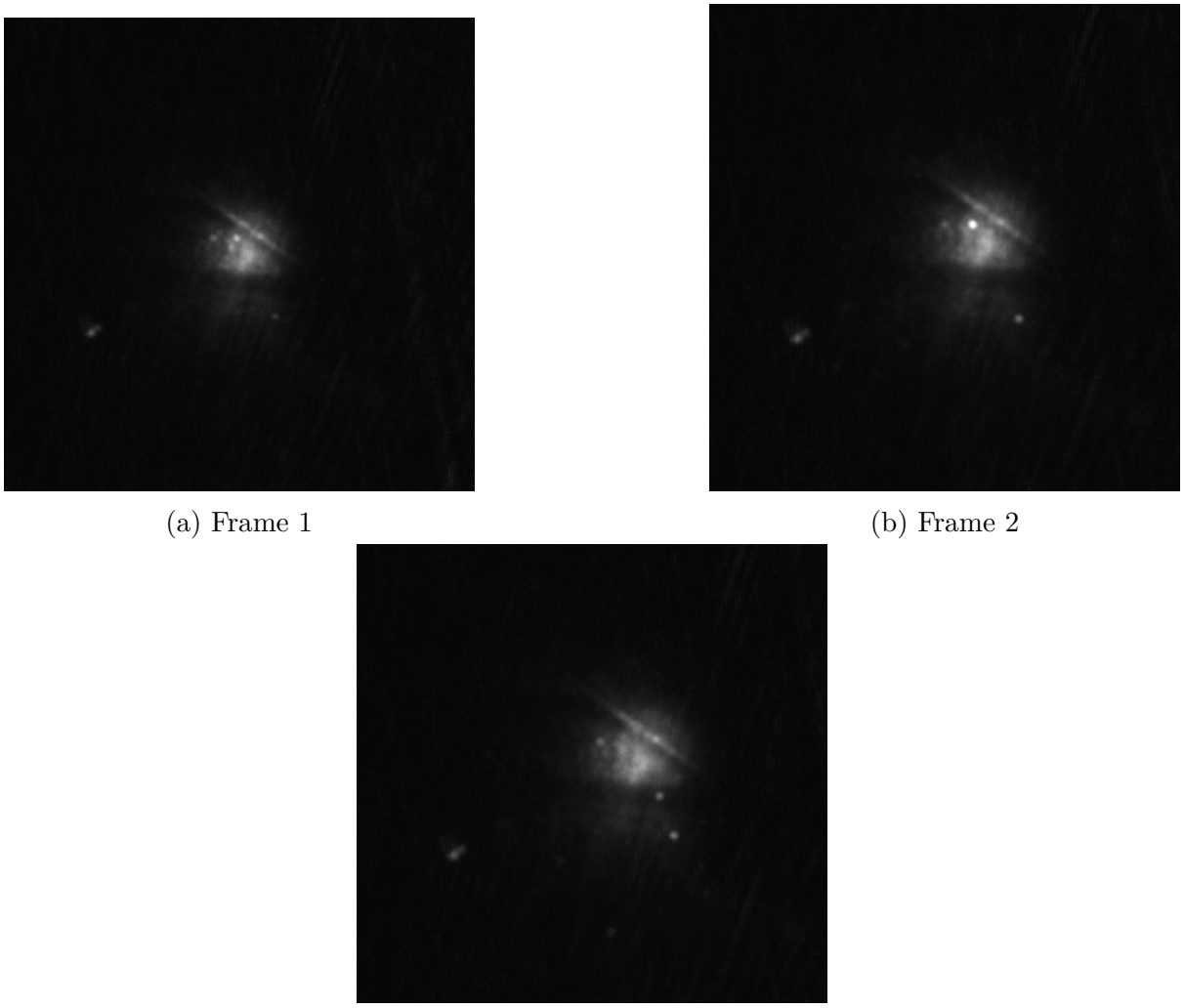

(a) Frame 1

(b) Frame 2

(c) Frame 3

Figure 4.18: Three consecutive frames of a video that depicts the luminescence's evolution coming from the flake in fig. 2.11.

for rapid coarse patterning and with an integrated feedback loop for in-situ imaging and markerless overlay alignment with lateral accuracy better than 25 nm.

Point-like modifications were performed by applying single thermal pulses with the NanoFrazor tip in direct contact with the hBN surface. During each writing event consisted the tip is locally heated, while maintaining a controlled contact force. The key writing parameters (tip temperature T_{tip}, dwell time t_{dwell}, and applied normal force F_{N}) are varied systematically to optimize defect formation without producing macroscopic damage. A 3x3 array of circles having a diameter of about 20 nm is designed to create point-like defects on 4 selected flakes.

In the following, the topography maps of the written regions on each flake are reported, along side the writing parameters. From fig. 4.20a we see that flake 1 has a well-defined faceted boundary in the upper-right region, and its interior appears significantly recessed, with depths reaching roughly –60 to –90 nm, suggesting either a deep terraced structure or

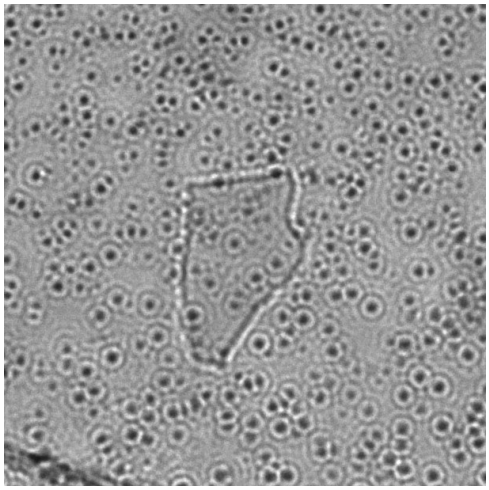

(a) Flake 1.

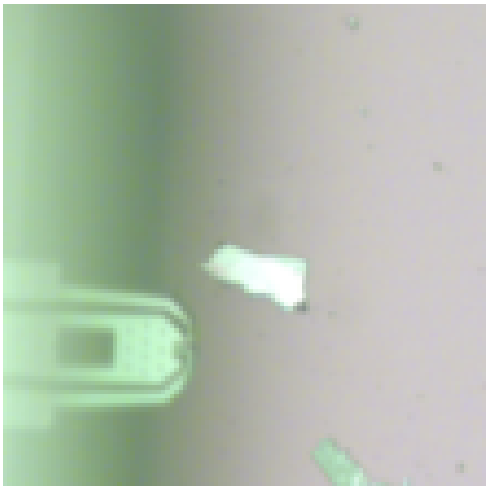

(b) Flake 2.

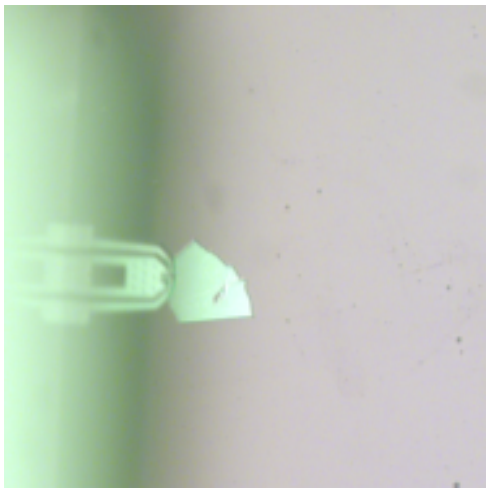

(c) Flake 3.

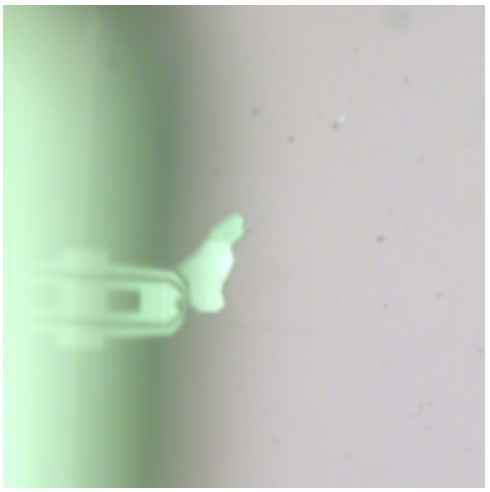

(d) Flake 4.

Figure 4.19: Some of the flakes aren't fully visible, since the AFM cantilever is also included in the picture. The first image appears different, because it was taken at the optical microscope, before using the Nanofrazor.

uneven transfer. The color gradient indicates a smooth but sloped surface across the flake, consistent with a wedge-like thickness variation produced during exfoliation. The shallow features and streaks are likely AFM scan artifacts or residual surface contamination. Localized bright spots correspond to small protrusions or debris particles. Overall, the image shows a partially delaminated or unevenly adhered flake. This region 4.20b shows a moderately thick portion of flake 2, with height variations up to 100 nm. The surface displays several internal terraces, suggesting uneven exfoliation and partial delamination. While this area 4.20c corresponds to a much thicker and more vertically structured section of flake 2, with depths exceeding 500 nm. The strong steps and broad terraces indicate overlapping layers or folded regions.

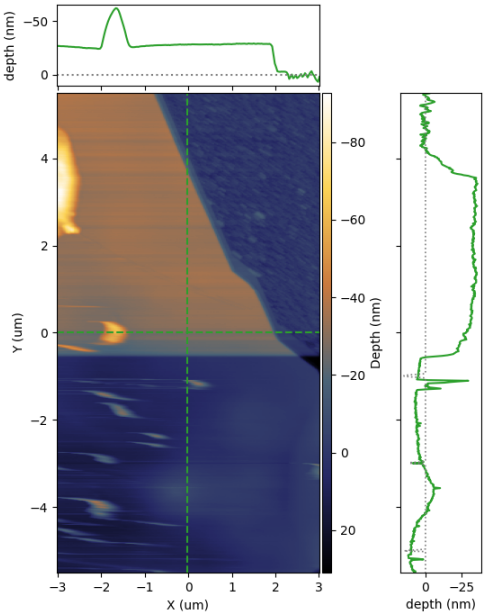

(a) Written on flake 1 with T_{tip} = 1200°C.

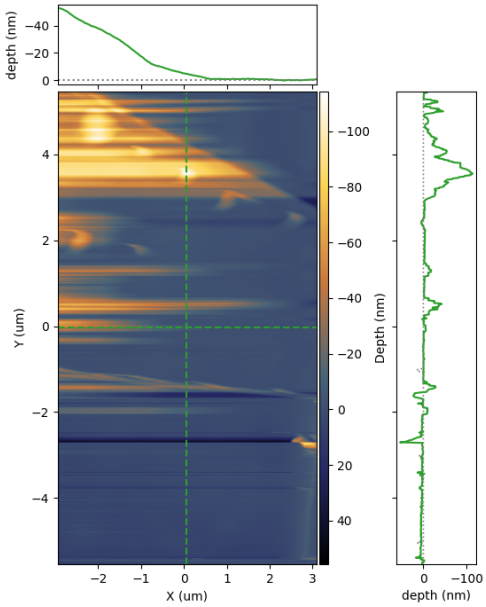

(b) Written on flake 2 with T_{tip} = 1250°C.

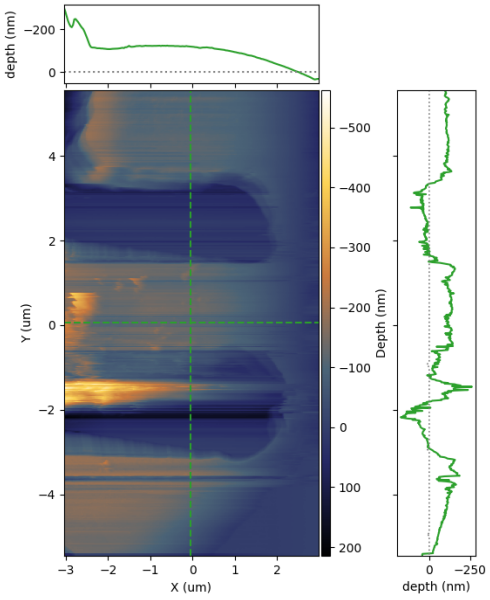

(c) Written on flake 2 with T_{tip} = 1300°C.

Figure 4.20: Writing events performed at a fixed t_{dwell} of 50 μs and 3 different tip temperatures T_{tip}.

Flake 3 instead appears to be overall thin, well-adhered, and relatively flat on the substrate, although in 4.21b we can clearly see a sharp, bright diagonal ridge, corresponding to a pronounced wrinkle or folded edge with a height of about 20–25 nm.

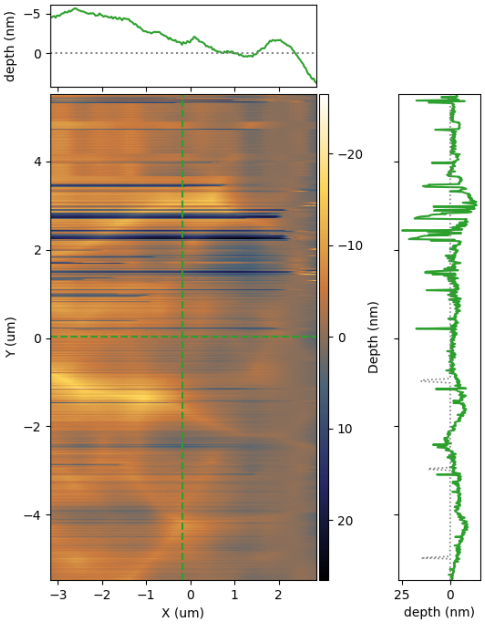

(a) Written on flake 3 with T_{tip} = 1200°C.

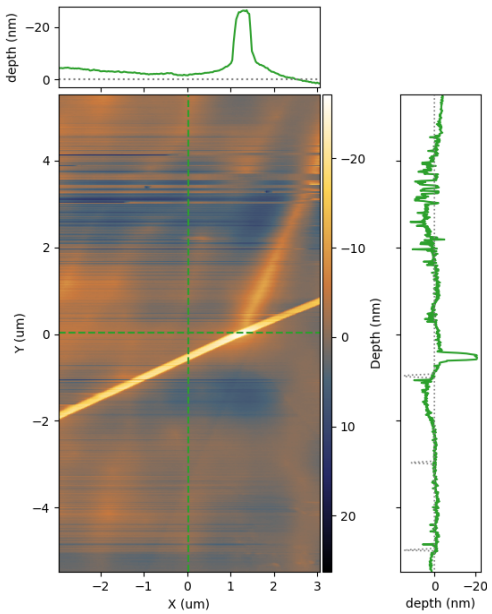

(b) Written on flake 3 with T_{tip} = 1250°C.

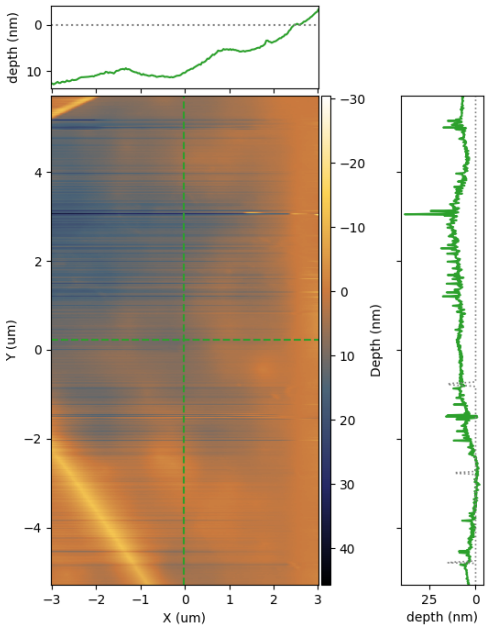

(c) Written on flake 3 with T_{tip} = 1300°C.

Figure 4.21: Writing events performed at a fixed t_{dwell} of 100 μs and 3 different tip temperatures T_{tip}.

This map 4.22a shows a portion of flake 4 featuring two pronounced vertical ridges, likely corresponding to folds or overlapping layers. These lines reach heights of about 20–30 nm, with small step-like modulations along their length that suggest local multi-layer segments or trapped residues. The surrounding surface is relatively flat. In this area 4.22b, three thinner and well-defined edges intersect, forming a local branching pattern. These features likely represent natural flake edges. This region 4.22c is the smoothest:

the topography is almost entirely uniform, with height variations typically below 10 nm. Only gentle, broad undulations are visible, indicating an area of the flake without prominent edges, possibly lying more relaxed and well-adhered to the substrate.

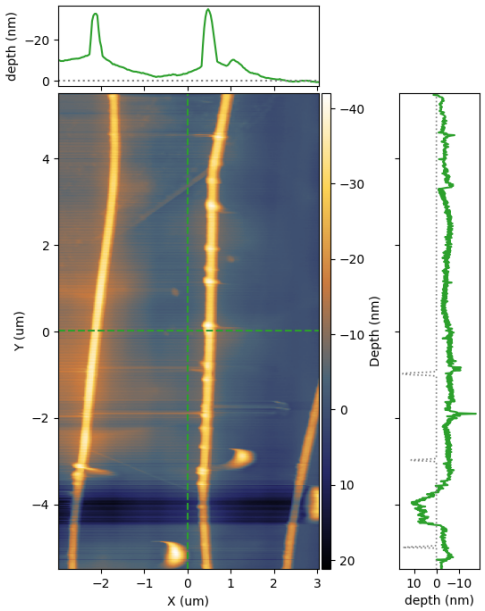

(a) Written on flake 4 with T_{tip} = 1200°C.

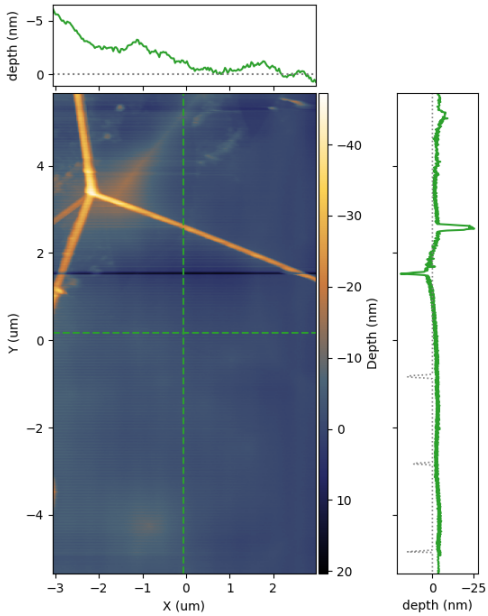

(b) Written on flake 4 with T_{tip} = 1250°C.

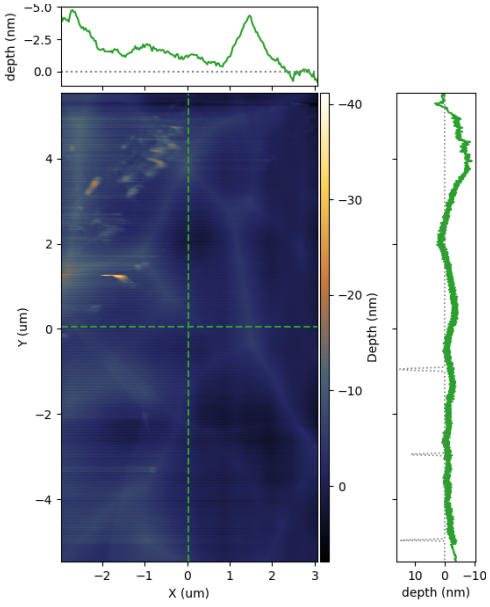

n

(c) Written on flake 4 with T_{tip} = 1300°C.

Figure 4.22: Writing events performed at a fixed t_{dwell} of 150 μs and 3 different tip temperatures T_{tip}.

The formation of point defects in hBN is expected to introduce localized electronic states within the wide hBN band gap (6.0 eV), enabling optical transitions in the visible

range (typically 550–800 nm). Thermal probe lithography allows deterministic control over the defect density and spatial positioning, with minimal contamination compared to electron-beam or ion irradiation methods.

4.3 Optical setup

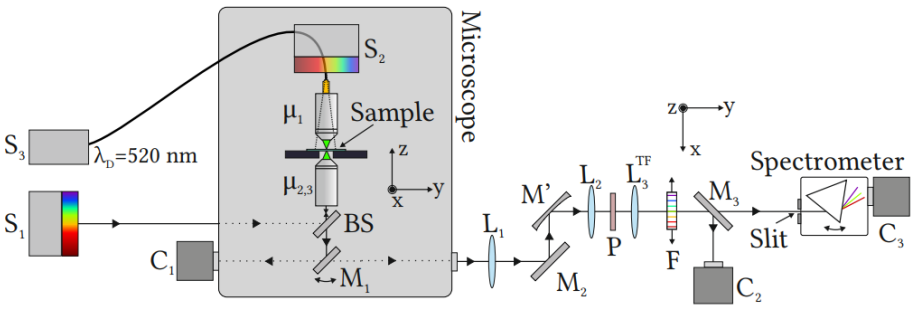

Figure 4.23: Experimental setup used to characterize the optical structure.[1]

The sample is mounted in a modified optical microscope that accommodates multiple illumination sources in both transmission and reflection geometries. A gooseneck white-light source, S_1, is introduced from the rear of the microscope, while the microscope's halogen lamp can serve as an alternative white-light source, S_2. A fiber-coupled laser diode, S_3, with wavelength $\lambda_D = 532$ nm, is coupled directly into a microscope objective μ_1 (20×, $\mathrm{NA}_{\mu_1} = 0.5$), permitting the laser to be tightly focused onto the investigated area.

In both reflection (S_1) and transmission (S_2 and S_3) modes, light is collected from beneath the sample by an objective μ_2 (40×, $\mathrm{NA}_{\mu_2} = 0.6$), which can be exchanged for a second objective μ_3 (100×, $\mathrm{NA}_{\mu_3} = 0.9$). The collected beam is routed through a beam splitter (BS) that enables simultaneous delivery of source S_1 to the sample and collection of light from all sources.

An internally mounted rotating mirror, M_1, directs light either to the microscope's built-in camera, C_1, for real-space imaging of the sample surface, or out of the microscope toward an external relay formed by lenses L_1 and L_2 and by flat or spherical mirrors (M_2 and M'). This external path provides magnification and beam steering through a polarizer P, a translation-mounted rainbow filter F, and a removable lens L_{TF3} that can be inserted to perform a Fourier transform of the image and thereby display intensity as a function of wave vector.

A removable mirror, M_3, switches the beam to either a second camera, C_2, for direct imaging of the back focal plane (BFP), or to a dispersion analysis branch. The dispersion arm contains a slit aligned along the z axis that selects wave-vector components in that direction; light passing the slit is dispersed by a spectrometer and projected onto a

camera, C_3, that is matched to the spectrometer. This arrangement enables acquisition of an entire dispersion diagram in a single exposure.

Two orthogonal coordinate systems are included in the schematic to clarify the geometry: the sample plane is parallel to the optical table (XY plane) and the downstream optical layout is shown from above. Finally, note that S_3, cameras C_1, C_2 and C_3 and the spectrometer are interfaced with a PC, and that rotation of the spectrometer prism permits selection of a spectral window of approximately 70 nm for dispersion imaging.

Chapter 5

Results and Discussion

In order to investigate the optical response of the multilayers, we shine a white light on them and measure both the dispersion of the Tamm plasmon mode and of the Bloch surface mode. The dispersion relation is obtained by performing angle-resolved reflectivity measurements, in which the reflected light is collected as a function of the incident angle. This technique allows one to directly probe the in-plane momentum of the confined mode, making it possible to reconstruct its dispersion. Then, we also want to measure the luminescence, excited by a green laser at 532 nm, coming from the hBN defects coupled to both the BSW and the TP.

5.1 Tamm plasmon dispersion

The measurements are first carried out on the bare sample, i.e. without any flake, using a white light lamp and an objective with numerical aperture $NA = n_{eff} = n_1 sin(\theta_{in}) = 0.9$, where $n_1 = 1$ is the air's refractive index and θ_{in} is the angle of incidence. In this case, the TP mode appears as a parabola-shaped dip in the reflectivity spectrum, located inside the light cone, in-between $n_{eff} = \pm 1$. We can then see, as a function of the wavelength, the characteristic dispersion curve of the Tamm plasmon, which has the same shape of the simulated one in fig. 2.7 but with inverted axes.
To assess the influence of hBN on the optical response, we repeat the same set of measurements after transferring some flakes of hBN onto the metal surface. The presence of this additional dielectric layer increases the overall scattering, leading to a fainter TP dispersion; moreover, it modifies the boundary conditions at the interface, leading to a shift of the TP dispersion (**dielectric loading**). However, this effect turns out to be negligible in our dispersion measurements. The mode maintains its spectral sharpness, confirming that the quality factor of the TP was preserved despite the introduction of the flake, since it's not a proper surface mode, but rather a near-surface mode.
We consider first a spot (fig. 5.1) and a flake (fig. 5.2) that are very close to the sample's

edge, whose dispersion appears to be quite shifted with respect to the simulation 2.7, probably because the sample's thickness decreases near the edges. We will later confirm this hypothesis by carrying out some other measurements.

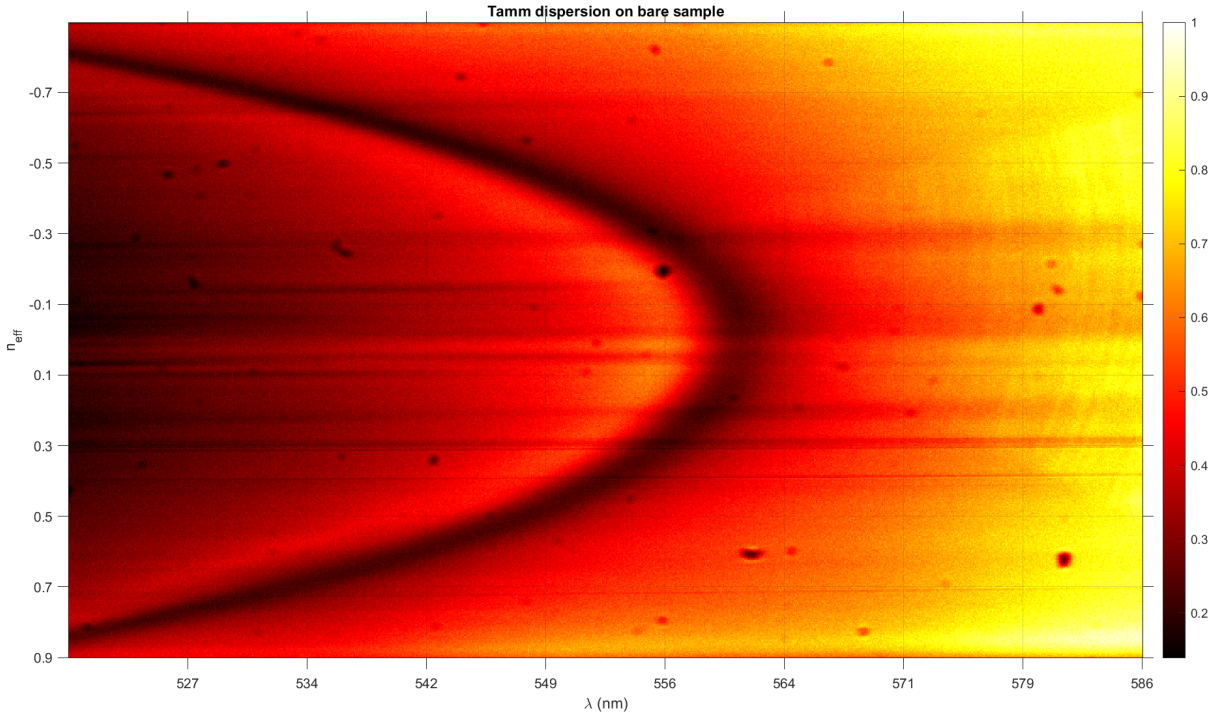

Figure 5.1: Tamm dispersion measured on the bare sample's edge.

By directly comparing the reflectivity maps measured with and without the hBN flake, we can thus clearly identify the impact of the additional dielectric environment on the Tamm plasmon mode.

Then, some other flakes are transferred on more central regions of the sample's surface, and the Tamm dispersion is measured once again. We report here (fig. 5.3 and 5.4) the reflectivity maps to make a comparison with the ones measured on the edge.

Now the obtained plots are much closer to the simulation's result, showing that our hypothesis about the blue-shift was correct; it's indeed due to the sample's edge being thinner with respect to the central area.

5.1.1 Fluorescence

After measuring the TP dispersion, we would like to observe the luminescence coming from the point-like defects, realized by means of the NanoFrazor, which should couple to the TP mode. Unfortunately, there's a strong background luminescence (visible also in the video frames 4.18) coming directly from the sample, which makes it impossible to localize the 3x3 array of point-defects. The reason for this could be impurities and damages to the sample's surface, but also the luminescence coming from the silver layer itself and from carbon residues. Nevertheless, it was shown previously [1] that coupling

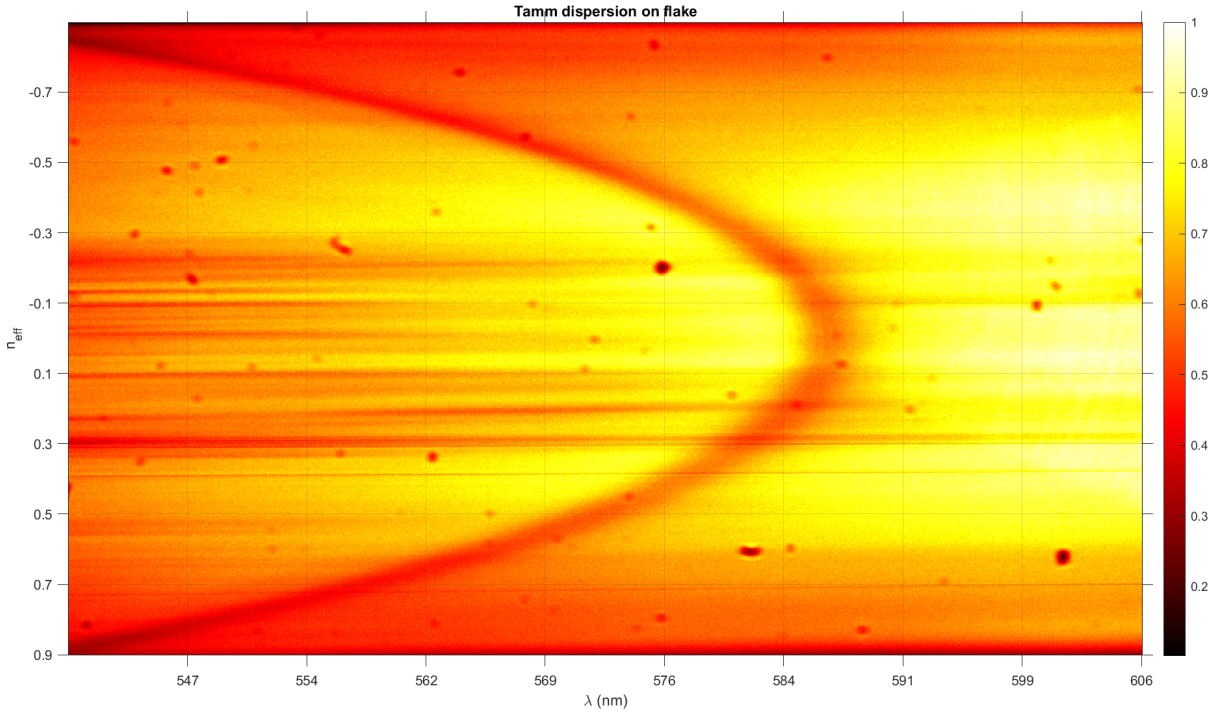

Figure 5.2: Tamm dispersion measured on a flake near the sample's edge. As we can see, the parabola appears brighter, because of the increased scattering, and its vertex is redshifted, going from about 560 nm to approximately 585 nm, but it's not due to the dielectric loading, as one could think. Actually, it's due to the strong non-uniformity near the sample's edge.

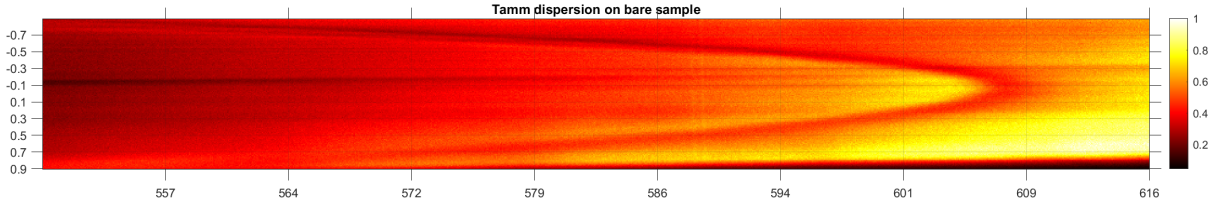

Figure 5.3: Tamm dispersion measured on the bare sample in a central area. Now the parabola's vertex is around 605 nm, a value much closer to the one predicted by the simulation. This result of coure is coherent with the one presented in [1] about the same Tamm structure.

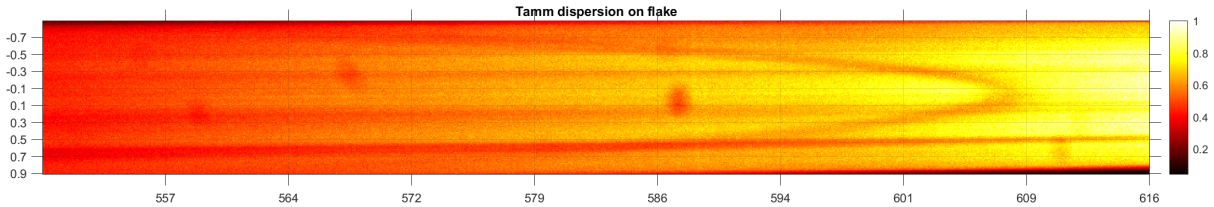

Figure 5.4: Tamm dispersion measured on a flake in a central area. As already discussed, the dielectric loading effect is negligible, since no redshift is observed.

between the TP mode and other possible SPSs, such as quantum dots (QD) is possible, using exactly the same Tamm structure with QDs fabricated on top of it.

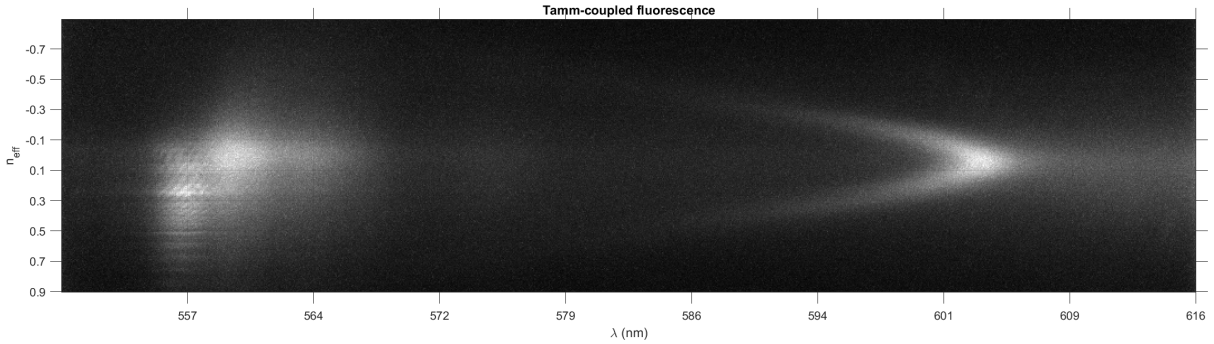

Figure 5.5: Tamm-coupled fluorescence coming from a QD, excited by a laser at 532 nm. The fluorescence, however, looks spectrally too broad to be an eligible SPS.

5.2 BSW mode

When a multilayer supports a BSW and its surface is patterned with a grating, illumination from above can couple free-space light to the BSW through the grating momentum. We know from the simulation 4.8 that the surface gratings, fabricated by means of EBL, should correctly couple to the BSW and diffract it along a non-planar direction; therefore, if we shine a white light on one of them, we should see the coupling and decoupling of the BSWs with the nearby gratings. This is very convenient, since it allows us to avoid the oil immersion working mode, overcoming the problem about the BSW dispersion's placement.
For all the following measurements the sample is placed face down on the microscope objective, and both illumination and light collection are from the bottom.

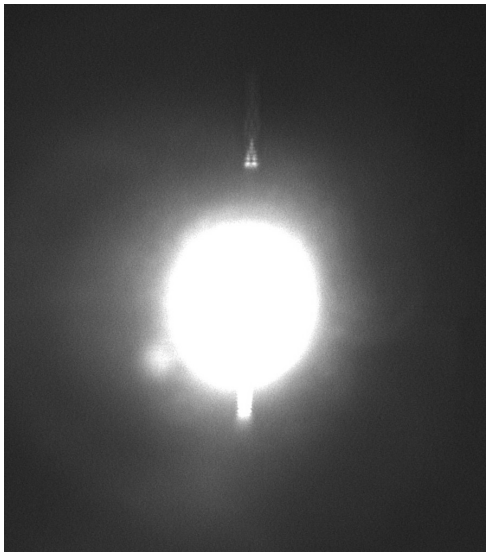

(a) The white light spot is shining on one grating, but also its neighbor is diffracting light, because it couples to the BSW mode.

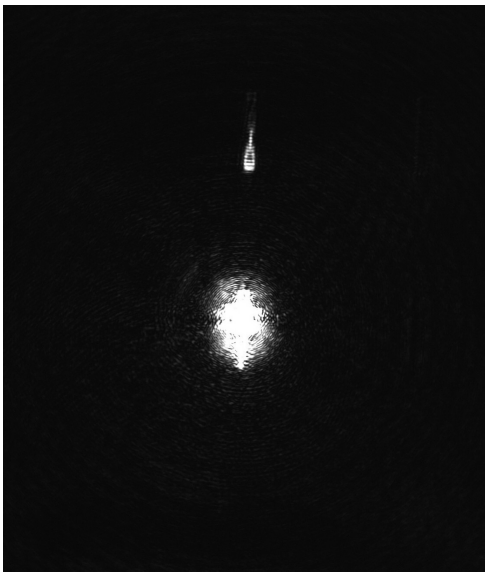

(b) Even when using the green laser at 532 nm we can observe the BSW-grating coupling.

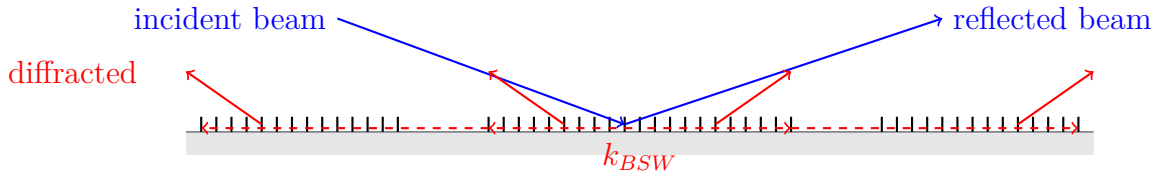

Figure 5.7: Schematic representation of the BSW excitation and diffraction by three surface gratings. A portion of incident light, belonging to the forbidden band, is immediately reflected back, while some of it matches the BSW energy and momentum; this couples to the central grating, and propagates (dashed red arrows) along the surface, up to the nearby gratings. The decoupling causes the BSW to be diffracted along a non-planar direction. The objective can therefore collect both the diffracted BSWs and the reflected light.

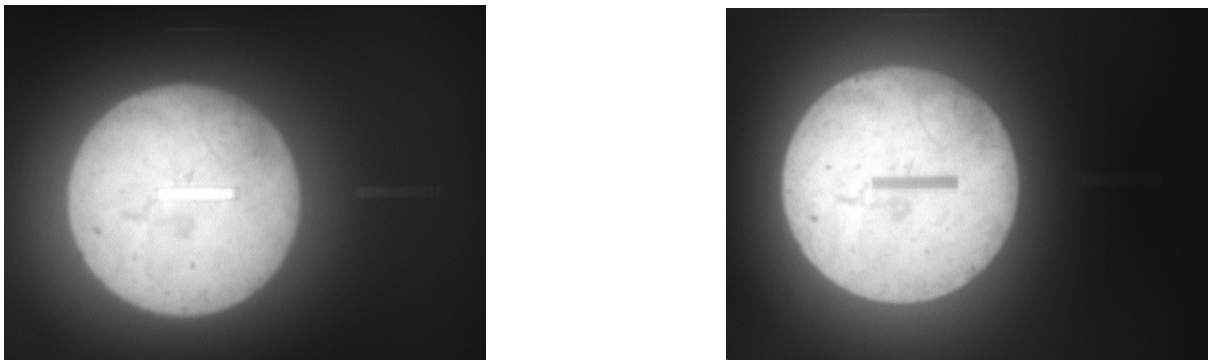

Figure 5.8: Since the BSW is TE polarized, we can see the gratings switching on and off, depending on the incident light's polarization. On the left TE, on the right TM.

5.2.1 Back-focal-plane reflection imaging of a grating-coupled BSW

Imaging the **back focal plane** (BFP) of the collecting objective, having a numerical aperture $NA = 0.9$, in reflection maps the angular distribution of the reflected light: each point in the BFP corresponds to a specific polar angle θ (and hence to an in-plane momentum component $k_{\parallel} = k_0 \sin\theta = \sqrt{k_x^2 + k_y^2}$). So, if we select a specific wavelength λ by means of an optical filter, we can observe the collected light in the $k_x - k_y$ plane; most of it comes from direct reflection, due to the forbidden frequency ranges, but also the diffracted BSWs are visible. Moreover, if we don't use any filter, it's impossible to distinguish anything on the BFP, which appears as a very bright spot, since the contribution of several wavelengths adds up. In summary, a bright ring in the BFP reflection image corresponds to a forbidden frequency range, a dark ring is for the propagating ones, while the BSW appears as a bright inverted arc, not because it's reflected back, but because it couples to the grating, which diffracts it along a non planar direction. Moreover, gratings of different period diffract the BSW at 532 nm along different directions, meaning that its position in the BFP changes; the larger the grating's period, the more distant the BSW will be from the BFP center.

We report here 5.9 the BFP images for each grating period (510 nm, 530 nm, 550 nm, 570 nm and 590 nm), while directly illuminating it. Notice that in these pictures there are two bright inverted arcs, corresponding to the two coupled and then decoupled BSW modes, propagating in opposite directions (the two red diffracted beams coming from the central grating in fig. 5.7). According to the simulation, the best coupling should be seen with the 530 nm grating, since the filter is at 532 nm, but of course the gratings aren't perfect and neither the filter is. In retrospect, we would have achieved a better coupling with a 490 nm grating probably, and the BSWs would have appeared in the center of the BFP.

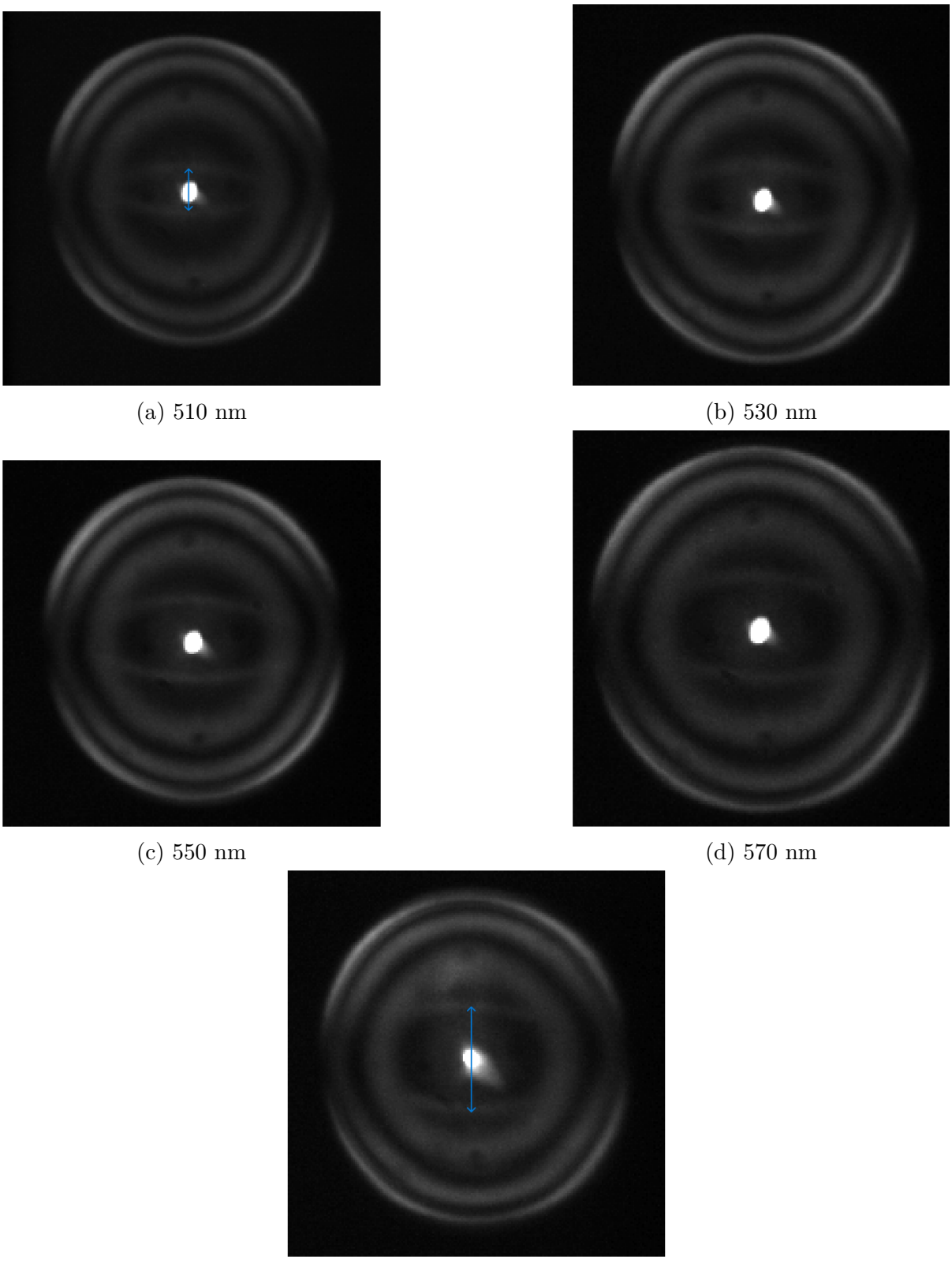

(a) 510 nm

(b) 530 nm

(c) 550 nm

(d) 570 nm

(e) 590 nm

Figure 5.9: The BSW appear to be more far away from the center as the grating's period increases. If they were to couple perfectly with one of the gratings, we would see both of them right in the center, which corresponds to normal diffraction. The largest diffraction angle is achieved with the 590 nm grating, while the smallest one corresponds 510 nm one, as highlighted by the arrows.

If instead we look at the BFP of the other two lateral gratings in fig. 5.7, we will see a single bright arc, but with opposite orientation depending on which grating we pick (fig. 5.11), since they're reached by opposite-propagating BSWs. Of course, with respect to the previous pictures, these images are a lot darker, since the objective isn't collecting all the light that is directly reflected back, but just the diffracted BSWs.

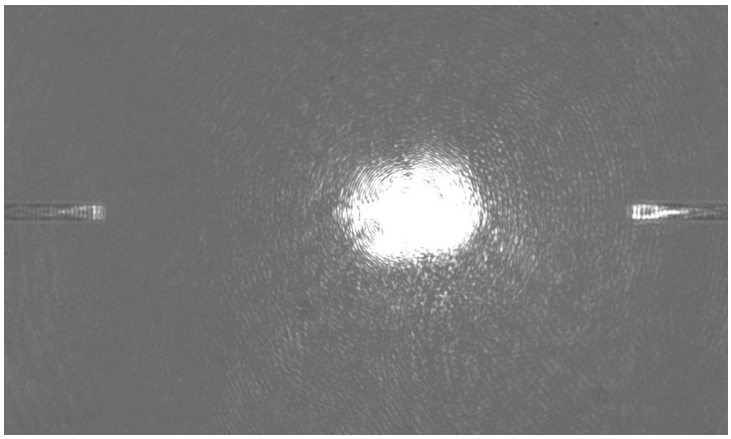

Figure 5.10: In this microscope picture we can see a situation identical to the one illustrated in fig. 5.7, where a central grating is illuminated by a laser at 532 nm and the other two nearby gratings are coupled to the BSWs.

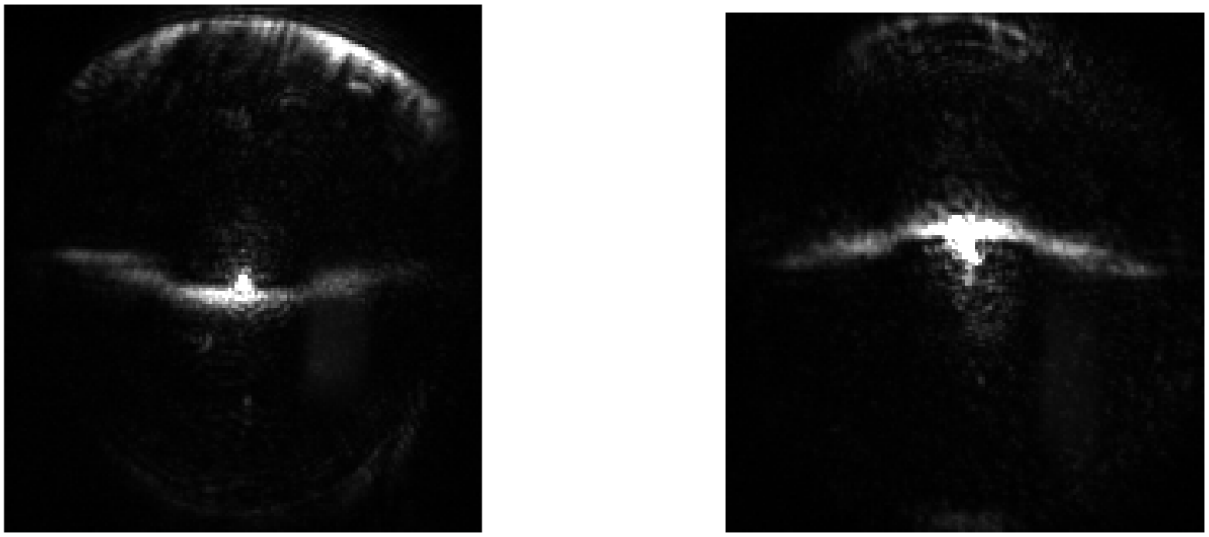

(a) (b)

Figure 5.11: BFPs of the left and right gratings in fig. 5.10.

5.2.2 BSW dispersion

To measure the BSW in the clearest possible way we should shine white light on one grating, and collect the light diffracted by its neighbor, which is just due to the coupled BSW. Unfortunately, our optical setup didn't allow for such configuration, so we had to give up on this idea, and instead we focused on measuring the BSW dispersion coming from the directly illuminated grating. In the following, we report the BSW dispersion measurements for each different grating. The BSW modes are marked by the 2 double-ended arrows, while all the other bright stripes are due to the reflected light.

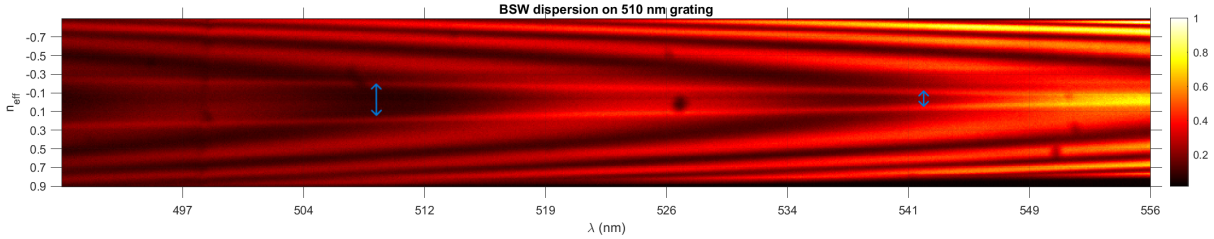

Figure 5.12: BSW measured on the 510 nm grating at 520 nm central wavelength.

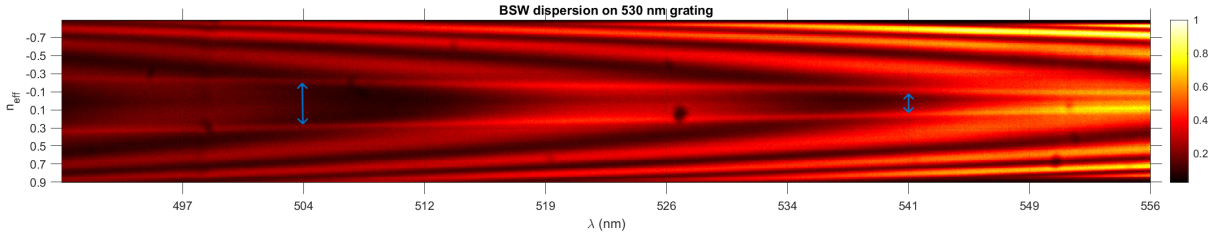

Figure 5.13: BSW measured on the 530 nm grating at 520 nm central wavelength.

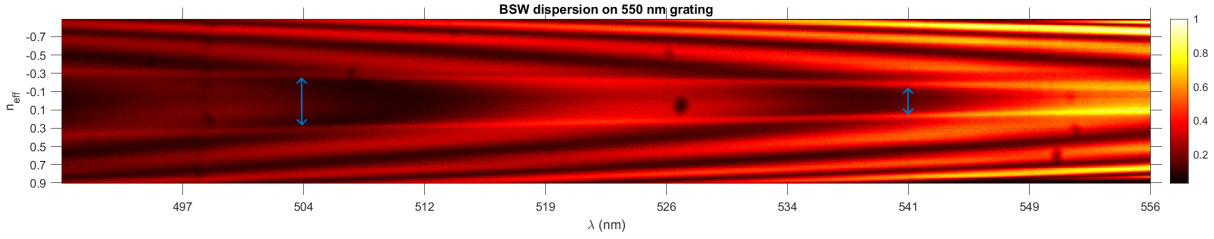

Figure 5.14: BSW measured on the 550 nm grating at 520 nm central wavelength.

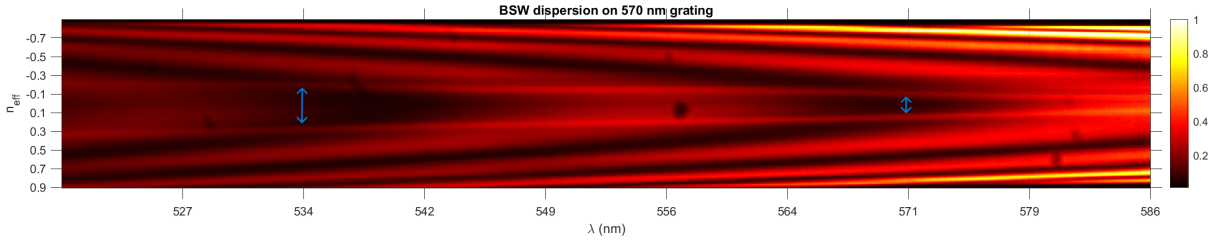

Figure 5.15: BSW measured on the 570 nm grating at 550 nm central wavelength. Notice the different wavelength range with respect to the previous 3 plots, since each grating is optimized to couple to light whose wavelength matches the grating's period.

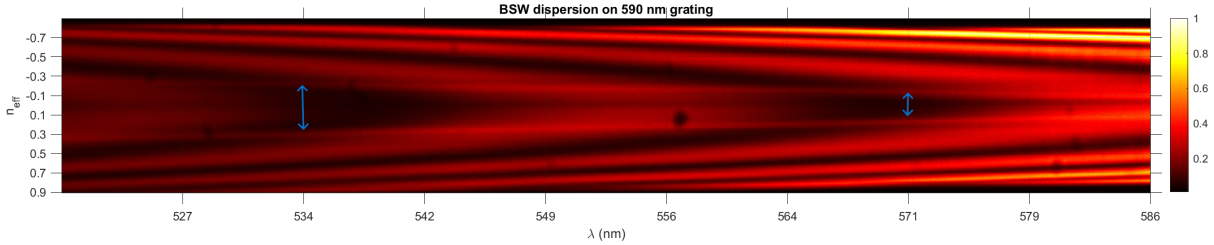

Figure 5.16: BSW measured on the 590 nm grating at 550 nm central wavelength.

5.2.3 Fluorescence

After transferring some hBN flakes, which ideally should fall in-between the gratings, we try to excite the fluorescence coming from hBN natural defects and the coupling to BSW mode. So, we shine a 532 nm green laser to excite the transition in hBN defects and perform spectral measurements.

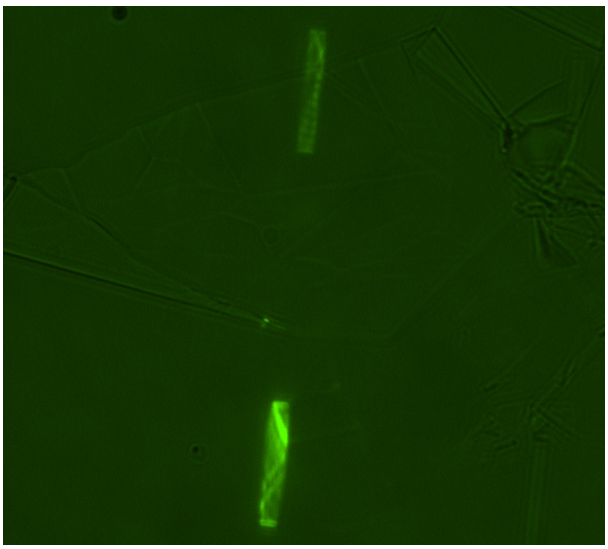

Figure 5.17: In this picture we can see two gratings and one big flake, partly falling on one of the gratings. The laser is focused on a very tiny spot of the flake, and it looks like there's a strong photoluminescence coupled to the BSW. After further measurements, however, we have to leave out this hypothesis, since there's no dependence on the polarization. It's probably just scattered light that gets to both gratings.

Several different flakes are analyzed, both thick and thin, lying in-between the gratings and on top of them, but no coupled luminescence is observed. To check the coupling condition, we add a polarizer to the optical path, since the BSW is TE polarized; no intensity change is observed by rotating the polarizer, so we can conclude that it isn't a BSW mode. Our guess is that there aren't any suitable natural point-like defects in the hBN flakes, so a possible solution could be to create them ad hoc, using AFM indentation or some other technique.
However, in absence of flakes, we can measure the very broad fluorescence coming from the grating's resist (fig. 5.18), which effectively couples to the BSW, and is indeed TE polarized.

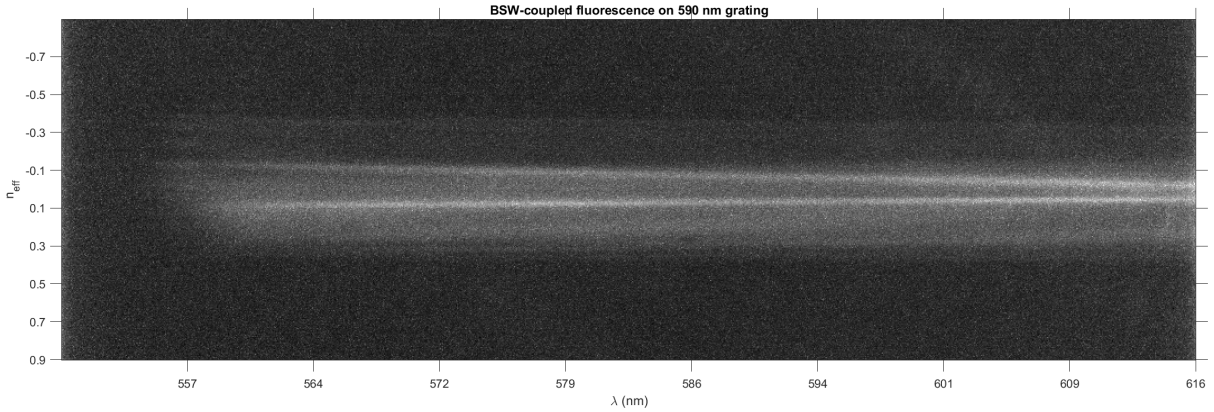

Figure 5.18: BSW-coupled fluorescence coming from the 590 nm grating. It's way too broad to be used as single photon emitter, but it clearly demonstrates that coupling is possible.

We can also make a comparison with the simulated reflectivity map of a top illuminated 590 nm grating 5.19, to show that the measured BSWs match quite well with the theoretical ones in fig. 5.20.

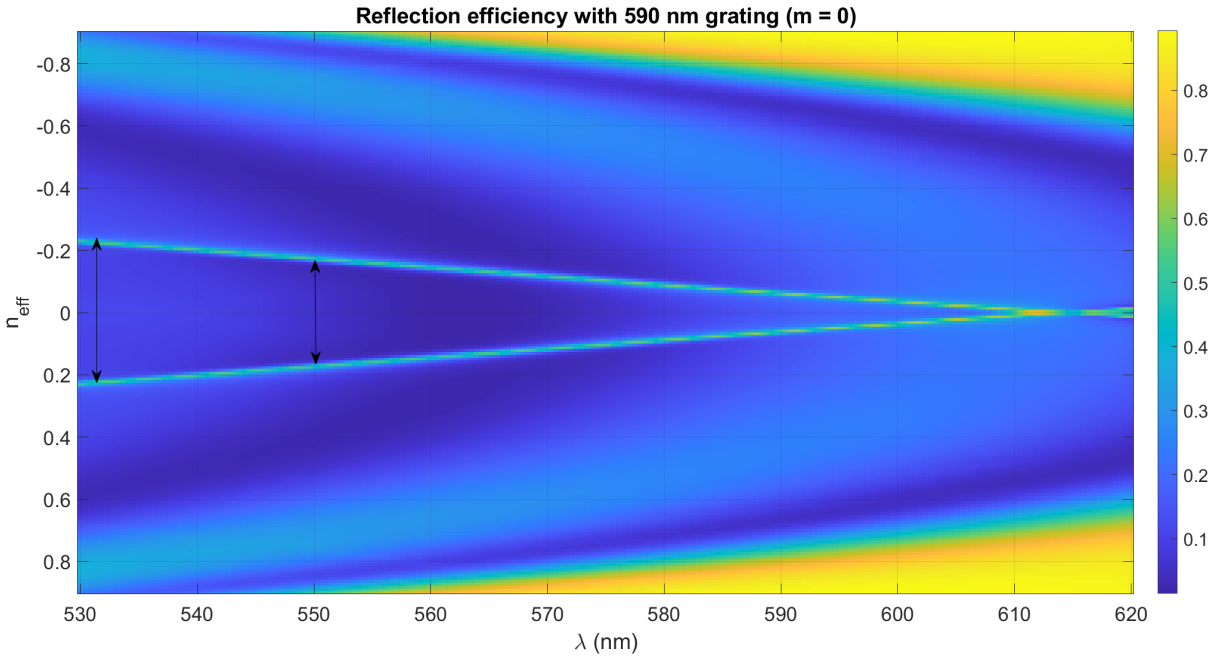

Figure 5.19: Reflection efficiency of a 590 nm grating with top illumination. The n_{eff} has been restricted to $[-0.9, 0.9]$ to faithfully reproduce the actual numerical aperture of our optical setup. Calculated by means of RETICOLO [3].

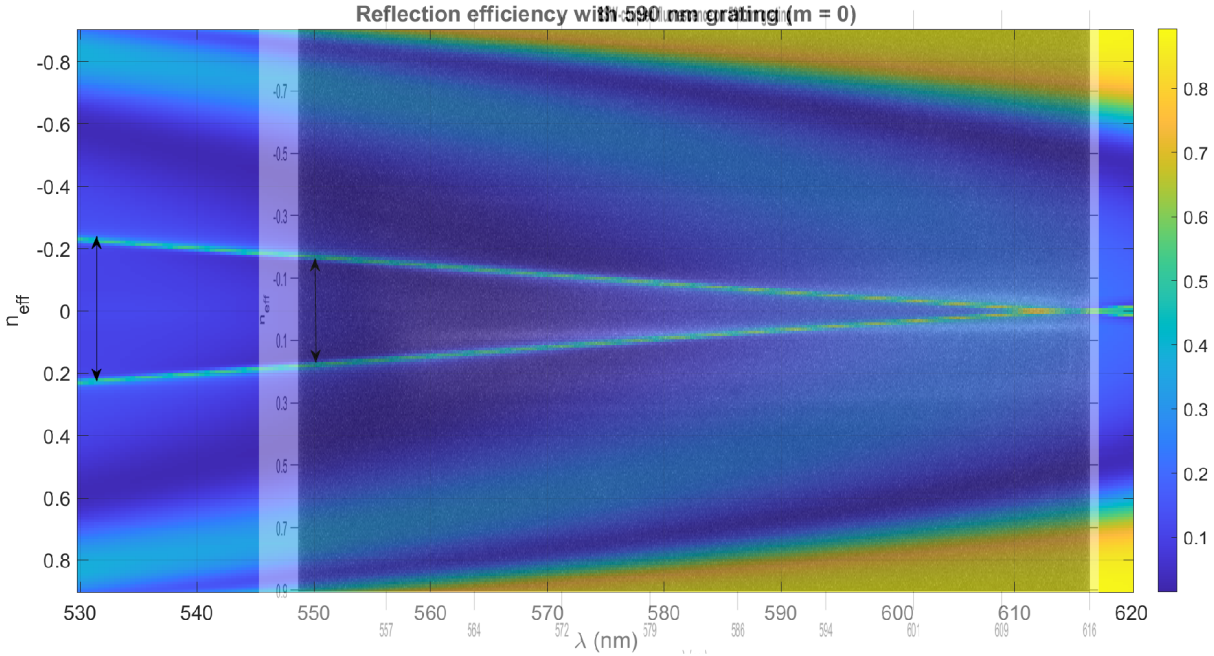

Figure 5.20: Superimposition of 5.18 and 5.19. The double-ended arrows mark two important λ: 532 nm, which is the filter's wavelength (used to take the BFP pictures), and 550 nm, the lowest wavelength that our optical setup can reach to perform spectral measurements.

Then, using the same simulation, we want to show that the distance between the two BSWs at 532 nm matches quite well the one in the 590 nm grating's BFP image, taken with a filter centered around the same wavelength.

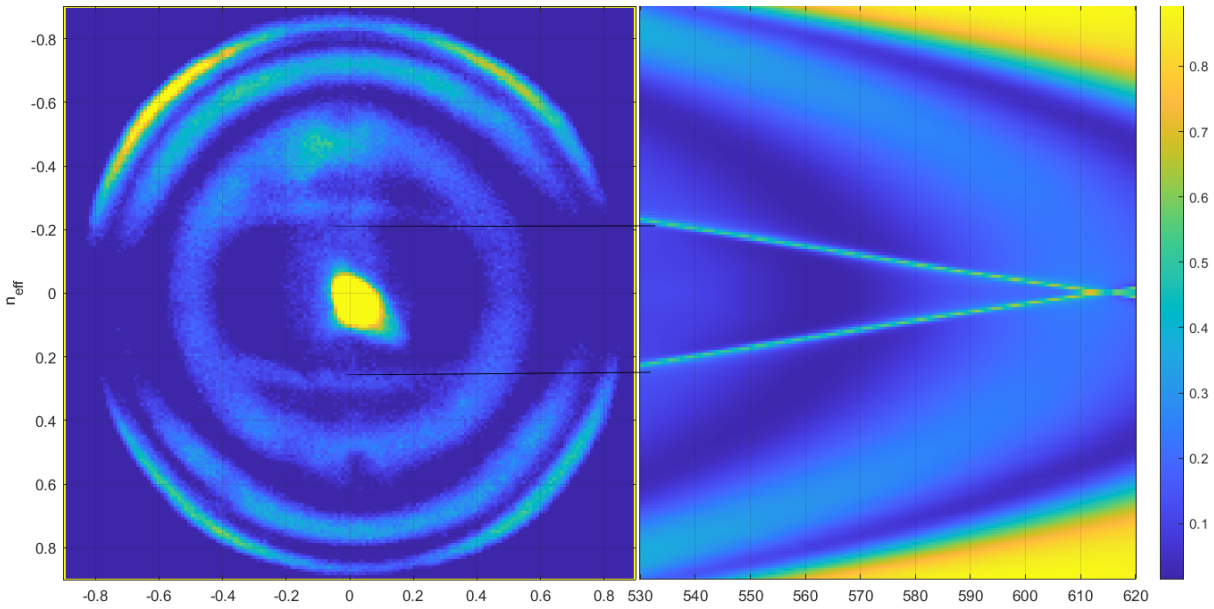

Figure 5.21: On the left there's the 590 nm grating BFP image, on the right there's the same plot of fig. 5.19. As we can see, the lower line, starting from the BFP, doesn't end exactly upon the BSW dispersion, so the alignment isn't perfect, but it can be considered a good match.

Overall, we can assert that the collected experimental data, both the BSW dispersion measurement 5.20 and the BFP image regarding the 590 nm grating 5.21, are conforming to the theoretical data.
Lastly, we would like to quantify the dielectric loading effect by measuring the BSW dispersion through a flake, lying directly on top of one of the gratings, and compare it with the previous plots. So, we switch back to white light, but now the BSW completely disappears, due to the disruptive scattering caused by the flake's presence. This result shows how much more fragile is the BSW mode with respect to the Tamm plasmon, being a true surface mode, which makes it way more sensitive to the surface's changes.

Chapter 6

Conclusions and Future Work

6.1 Conclusions

This thesis explored the integration of defect-based emission in hexagonal boron nitride with optical modes sustained by engineered multilayer structures, with particular focus on Tamm plasmons and Bloch surface waves. Through a combination of electromagnetic simulations, nanofabrication, and optical measurements, the work aimed to assess whether such hybrid platforms could improve the efficiency and directionality of emission from hBN flakes.

Tamm plasmon modes were successfully observed both in simulations and in experiments on the bare multilayer. Their characteristic dispersion was retrieved with good agreement, and measurements revealed that the presence of hBN introduces only a negligible perturbation to the TP resonance. This observation confirms the robustness of Tamm plasmons, which, being near-surface rather than true surface modes, are only weakly affected by dielectric loading effects.

Conversely, the Bloch surface wave platform exhibited more delicate behaviour. BSW dispersion was reproduced experimentally using grating-coupling techniques, and the TE-polarized nature of the mode was verified. However, the introduction of hBN flakes severely degraded the BSW, whose visibility was strongly reduced or completely suppressed due to scattering introduced by flake roughness, folds, and inhomogeneities. This highlights the high sensitivity of surface-bound modes to surface perturbations.

Regarding defect-related fluorescence in hBN flakes, no clear signature of localized emission coupled to either TP or BSW modes was observed. The primary limitations were the low density of natural emitters in exfoliated flakes and the presence of strong background fluorescence from the multilayer and resist. Nonetheless, BSW-coupled fluorescence originating from the grating's resist demonstrated the viability of the coupling mechanism itself.

Overall, while deterministic defect activation and improved flake quality remain nec-

essary steps, the results confirm that both multilayer platforms are suitable candidates for integrating hBN-based emitters into compact photonic architectures.

6.2 Future Work

Several developments could significantly advance the integration of hBN emitters with multilayer structures:

- **Deterministic creation of emitters.** Thermal probe lithography has demonstrated promising control over defect formation, but optimization of dwell time, tip temperature, and flake quality is required to produce bright, spatially isolated emitters.
- **Improved transfer techniques.** The dry-transfer approach adopted here is simple but inefficient and prone to contamination. Methods such as temperature-controlled PDMS–PVC transfer [7] may yield cleaner flakes and higher transfer fidelity.
- **Reduction of background fluorescence.** Minimizing carbon residues, optimizing metal deposition, and performing gentle surface cleaning would help reveal weak defect luminescence.

By addressing these aspects, future research may unlock a reliable pathway toward hybrid hBN–multilayer devices that combine room-temperature operation with high emission control, enabling their implementation in practical quantum communication and information-processing systems.

Bibliography

[1] Lilian Emonin. Single-photon sources integrated at the tip of an optical fiber. *Second Year Research Internship Report*, Photonics, micro-nanotechnology, time-frequency metrology, and complex Systems (PICS), 2024-2025.

[2] Heidelberg Instruments Nano AG. *NanoFrazor – Thermal Scanning Probe Lithography Platform*, 2025. https://nanofrazor.com/nanofrazor/.

[3] Jean Paul Hugonin and Philippe Lalanne. Reticolo software for grating analysis. 2025. URL https://arxiv.org/abs/2101.00901.

[4] M. Kaliteevski, I. Iorsh, S. Brand, R. A. Abram, J. M. Chamberlain, A. V. Kavokin, and I. A. Shelykh. Tamm plasmon-polaritons: Possible electromagnetic states at the interface of a metal and a dielectric bragg mirror. *Phys. Rev. B*, 76:165415, Oct 2007. doi: 10.1103/PhysRevB.76.165415. URL https://link.aps.org/doi/10.1103/PhysRevB.76.165415.

[5] Satoshi Kishimoto. Electron moiré method. *Theoretical and Applied Mechanics Letters*, 2, 01 2012. doi: 10.1063/2.1201101.

[6] Niccolò Marcucci. Functional patterning of dielectric multilayers supporting bloch surfaces waves. 2023. URL https://hdl.handle.net/11583/2982692.

[7] Mohammad Nasimuzzaman Mishuk, Mouli Hazra, Anand Kumar, Peter Dannberg, Aslı Çakan, and Tobias Vogl. All-dry pick-up and transfer method for quantum emitter arrays in hexagonal boron nitride, 2025. URL https://arxiv.org/abs/2502.21111.

[8] M. G. Moharam, Eric B. Grann, Drew A. Pommet, and T. K. Gaylord. Formulation for stable and efficient implementation of the rigorous coupled-wave analysis of binary gratings. *J. Opt. Soc. Am. A*, 12(5):1068–1076, May 1995. doi: 10.1364/JOSAA.12.001068.

[9] C J R Sheppard. Approximate calculation of the reflection coefficient from a stratified medium. *Pure and Applied Optics: Journal of the European Optical Society Part A*, 4

(5):665, sep 1995. doi: 10.1088/0963-9659/4/5/018. URL https://dx.doi.org/10.1088/0963-9659/4/5/018.